



**GEOLOGICAL SURVEY OF CANADA  
OPEN FILE 7462**

**Alteration within the basement rocks associated with the P2  
fault and the McArthur River uranium deposit,  
Athabasca Basin**

**E.E. Adlakha, K. Hattori, G. Zaluski, T. Kotzer and E.G. Potter**

**2014**



Natural Resources  
Canada

Ressources naturelles  
Canada

**Canada**



**GEOLOGICAL SURVEY OF CANADA  
OPEN FILE 7462**

**Alteration within the basement rocks associated with the P2  
fault and the McArthur River uranium deposit,  
Athabasca Basin**

**E.E. Adlakha<sup>1</sup>, K. Hattori<sup>1</sup>, G. Zaluski<sup>2</sup>, T. Kotzer<sup>2</sup> and E.G. Potter<sup>3</sup>**

<sup>1</sup> Dept. Earth Sciences, University of Ottawa, 140 Louis Pasteur, Ottawa, Ontario

<sup>2</sup> Cameco Corporation, 2121 – 11<sup>th</sup> Street West, Saskatoon, Saskatchewan

<sup>3</sup> Geological Survey of Canada, 601 Booth Street, Ottawa, Ontario

**2014**

©Her Majesty the Queen in Right of Canada 2014

doi:10.4095/293364

This publication is available for free download through GEOSCAN (<http://geoscan.ess.nrcan.gc.ca/>).

**Recommended citation**

Adlakha, E.E., Hattori, K., Zaluski, G., Kotzer, T., and Potter, E.G., 2014. Alteration within the basement rocks associated with the P2 fault and the McArthur River uranium deposit, Athabasca Basin; Geological Survey of Canada, Open File 7462, 35 p. doi:10.4095/293364

Publications in this series have not been edited; they are released as submitted by the author.

## ABSTRACT

The P2 reverse fault in the Athabasca Basin was a conduit for basinal fluids to enter the basement rocks below the regional unconformity and modify the rocks through fluid-rock interactions. Along the P2 fault, the basement rocks consist predominately of graphitic metapelite with quartzite and pegmatite. Immediately below the unconformity is an alteration profile consisting of a lower Green Zone with chlorite and illite, middle Red Zone dominated by hematite and kaolinite, and a discontinuous Bleached Zone of kaolin-group minerals and illite right at the unconformity. Preliminary data suggest that the alteration profile cannot be attributed solely to paleo-weathering but rather must include multiple fluid events from paleo-weathering through diagenetic to late hydrothermal fluids.

## INTRODUCTION

The P2 reverse fault is a relatively minor regional structure in the southeastern Athabasca Basin yet is spatially associated with the McArthur River deposit, the largest high-grade uranium deposit discovered to date. Whereas a few low-grade deposits, such as the P2 Main and minor uranium occurrences have been found along the P2, the McArthur River deposit is the only economic deposit discovered to date. The Zone 2 ore body of the McArthur River deposit is almost entirely hosted in basement rocks below Athabasca Basin; therefore, it is classified as a basement-hosted unconformity-type uranium deposit. The rocks adjacent to the P2 fault and below the Zone 2 ore body show evidence of extensive fluid-rock interaction as they are highly brecciated and altered. Therefore, the P2 fault may have served as a fluid pathway for uraniferous fluids to permeate the basement rocks and precipitate the ore.

This study began in the fall of 2012 and serves to explore the role of the P2 fault in the sub-Athabasca Basin during the uranium mineralization event at McArthur River in order to constrain the composition and source of the mineralizing fluids and identify fertile alteration. The outcomes of this study may be useful in discriminating fertile structures from the multiple generations of minor faults in the area and in targeting favourable areas for mineralization along the P2 and similar structures in the Athabasca Basin. The project is taking a systematic approach to studying the alteration of the basement rocks below the basin by describing and comparing the chemistry and paragenetic sequences of alteration minerals in the basement rocks below the basin in general, along the P2 reverse fault in the basement, and along the P2 fault proximal to uranium mineralized vs. non-mineralized rocks. This paper describes the preliminary findings from the first year of study and includes detailed petrography and major element chemistry of alteration minerals.

## GEOLOGICAL SETTING

### *Regional Geology*

The basement rocks below the eastern Athabasca Basin are part of the Wollaston Supergroup and host the Zone 2 ore body of the McArthur River deposit (Fig. 1). The Wollaston Group here consists of pelite, semipelite, arkose, calcsilicate and quartzite that were metamorphosed during the Trans-Hudson Orogeny (ca. 1.8-1.9 Ga; Lewry and Sibbald, 1980) under upper amphibolite facies conditions. Granitic pegmatite lenses intrude the metasediments and likely formed from local partial melting during peak metamorphism (Annesley et al., 2005). Substantial erosion during the exhumation of the basement rocks beginning at ca. 1.73 Ga resulted in weathering of the basement before the deposition of the Athabasca Group conglomerate and sandstone sequences (Kyser et al., 2000). The Athabasca Group comprises four major sequences of dominantly fluvial to marine, quartz pebble conglomerate

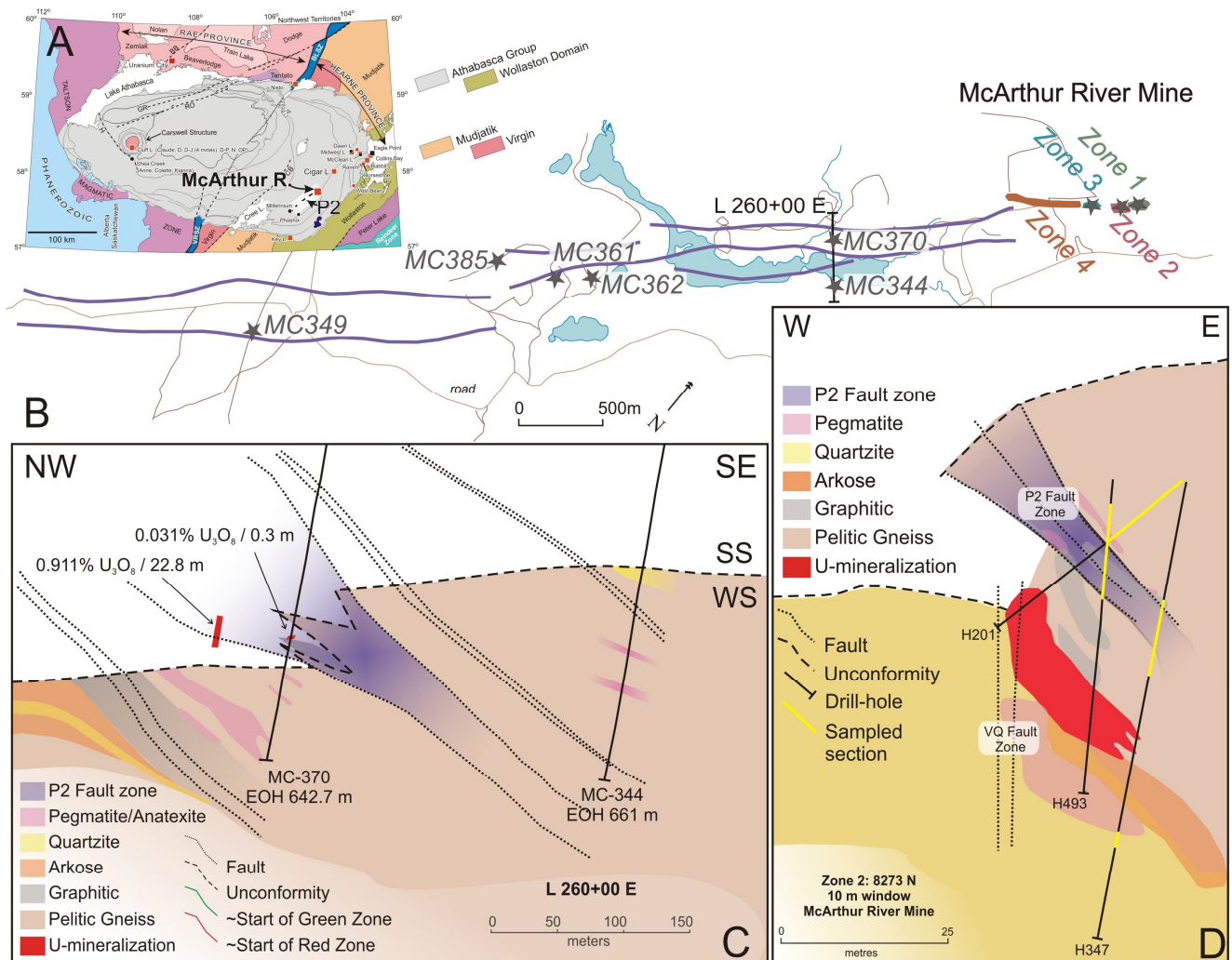


**Figure 1:** **A)** Map of the Athabasca Basin showing the locations of high-grade uranium deposits and major structural features, including the P2 reverse fault (highlighted in white) (adapted from Jefferson et al., 2007). **B)** Plan-view map showing the surface expression of the P2 fault in purple, access roads in brown, collars of diamond drill holes sampled for this study, and the McArthur River mine site. **C)** Cross-section of exploration line 260+00 E shows sampled drill holes MC-370 and MC-344 in geological context. **D)** An underground cross-section (8273N; 10 m window) of the Zone 2 from McArthur River Mine showing sampled drill-holes H201, H347 and H493 (sampled areas highlighted in yellow). The Zone 2 cross-section was interpreted by this author based on drill-core logs and cross-sections provided by Cameco. Plan-view map and cross-sections are adapted from the Bronkhorst et al. (2012). SS = sandstone; WS = Wollaston Supergroup.

and quartz-dominated sandstone (99% quartz framework grains with minor K-feldspar + clay matrix), currently preserved at a maximum thickness of 1500 m in the centre of the basin (Ramaekers et al., 2007).

### *Geological Setting of the McArthur River deposit and structure of the P2 fault*

Above the McArthur River deposit, the thickness of the conglomerate-sandstone succession is approximately 500 m. Some conglomerate and sandstone units have been intensely silicified (Hiatt and Kyser, 2007; Matthews et al., 1997). During and after deposition of the Athabasca Group, diagenetic fluids extensively altered much of the stratigraphic section (except for the intensely silicified units), as well as the basement rocks close to the unconformity. Subsequent hydrothermal activity further altered and brecciated these rocks, particularly along intersecting faults that provided

the fluid pathways. Breccias host ore pods along the ~050° P2 fault, the Vertical Quartzite (VQ) fault, and ~140° trending cross faults (Fig. 1).

The main ore body at McArthur River is termed Zone 2, hosted by the P2 reverse fault and bounded by the vertical quartzite (VQ) fault in the basement rocks. The deposit is classified as unconformity-type because it is located at the basal unconformity (~500 m depth) between the Athabasca Group and underlying metamorphic basement rocks (Fig. 1D). The primary mineralization event for the Zone 2 ore body was dated at  $1521 \pm 8$  Ma with subsequent remobilization at  $1348 \pm 16$  Ma (U-Pb on uraninite, McGill et al., 1993). The P2 fault zone preserves a record of multiple reactivations with a subtle to 80 m net reverse offset of the basal unconformity that placed the basement rocks above the basal conglomerate and sandstone units (McGill et al. 1993). In the basement the P2 fault is hosted within graphite-bearing metapelite and can be traced seismically as a listric structure down at least 2 km and laterally some 1.5 km (Hajnal et al., 2007). In the sandstone the P2 splays into multiple faults that flatten toward sub-parallelism with bedding (McGill et al., 1993). Hydrothermal alteration has been documented to be structurally controlled along the P2 fault zone, as alteration occurs along the shear zone, splay faults, and fractures (Jefferson et al., 2007). The VQ fault is a steeply dipping structure located between the footwall quartzite and cordierite-bearing pelite (source?).

## PREVIOUS RESEARCH

### *Regional and district-scale alteration*

Macdonald (1980; 1985) examined the alteration of the basement rocks and identified four zones in the regolith. He considered the lower three zones to be analogues for deep lateritic profiles that developed under sub-tropical climate and the upper zone created by the reaction of the regolith with diagenetic fluids from the overlying basin. The four zones are as follows (listed in order of closest proximity to the unconformity):

- i) Bleached zone along the unconformity characterized by white, buff, pale yellow and green clay (predominately kaolinite) that replaced all primary minerals except quartz, and was generated by a reducing diagenetic fluid,
- ii) Hematite zone (akin to a laterite zone) that varies from 2 – 12 m thick where hematite replaced all mafic minerals (predominately biotite),
- iii) Discontinuous White zone (pallid zone) that only forms in felsic units and where white clay replaced feldspar and dark green-black mafic minerals,
- iv) Green/Red Zone (saproilite zone) where feldspar was replaced by light green, yellow or pink/red clay (partially illitized), and mafic minerals were altered to green to dark-green/black (Mg-Al chlorite + illite).

Macdonald (1980; 1985) also investigated the bulk rock geochemistry of the different zones and noted that Fe (III) concentrations increase with proximity to the unconformity, whereas alkalis and Mg decrease. He attributed the Mg-Al chlorite in the Red/Green zone to be a product of burial metamorphism beneath the Athabasca Group from a former smectite + illite assemblage, as chlorite does not form under weathering conditions. He also speculated that the Bleached zone formed from a later reducing diagenetic fluid because the Bleached zone replaces the hematite alteration (oxidization) along the lower Hematite zone. Finally, as the trace element enrichment pattern in the Bleached zone are similar to that which accompany uranium mineralization (V, Mo, Pb, Ag, Ni, Co, and As), Macdonald (1980; 1985) speculated that mineralization and related alteration were generated by a diagenetic fluid under reducing conditions.

According to Alexandre et al. (2005), for the McArthur River, Rabbit Lake and Dawn Lake deposits, alteration around these basement-hosted unconformity-type deposits progressed in three stages:

- i) a “pre-ore” stage illitized plagioclase, crystallized chlorite in voids created by illitization and chloritized biotite, and pseudomorphic replacement of illite by chlorite proximal to mineralization,
- ii) a “syn-ore” event crystallized massive uraninite and coarse-grained illite in voids that were formed by pre-ore alteration, and
- iii) a “post-ore” stage remobilized and recrystallized uraninitite, crystallized spherulitic dravite in voids and chlorite in veinlets, and formed kaolinite, minor carbonate, drusy quartz, disseminated sulfides and fine-grained hematite.

Quirt (2012) compared basement clay alteration mineralogy below the Athabasca and Thelon Basins and provided important insights in recognizing retrograde (Fe-Mg) vs. prograde hydrothermal (Al-Mg) chlorite, and diagenetic (1Mc) illite vs. later mineralization-related diagenetic-hydrothermal (1Mt) illite. He interpreted retrograde chlorite from the waning stage of metamorphism as characterized by Fe-Mg rich chlorite (compositions intermediate between clinochlore and chamosite), whereas prograde hydrothermal chlorite is of the sudoite variety and replaced earlier formed Fe-Mg chlorite. Different illite generations, such as pseudomorphic replacements and open-space filling grains, are chemically similar and cannot be distinguished. Distinction between diagenetic vs. hydrothermal illite in the Athabasca Group sandstone is possible using scanning electron microscope-back scattered electron (SEM-BSE) imaging: diagenetic illite occurs as fine-grained plates whereas hydrothermal illite has a lath-like “hairy” habit and replaces earlier diagenetic illite. However, in the basement rocks hydrothermal illite (1Mt) replaces paleo-weathering clay minerals and has a more platy habit with fewer “hairy” whisps. Finally he noted that X-ray diffraction (XRD) can distinguish polytypes of illite.

District-scale alteration haloes that overprint the background dickite alteration in the Athabasca Group and that surround Athabasca U-deposits are summarized by Jefferson et al. (2007). A 10 – 20 km wide by 100 km long anomalous illite “corridor” trends north-east between Key Lake and Cigar Lake (Earle and Sopuck, 1989) and contains sub-parallel, narrower, anomalous chlorite and dravite zones. All the uranium deposits in the south-eastern part of the Basin, such as Key Lake and McArthur River, are located within this corridor. The timings of main mineralization events are uncertain because dates obtained on uraninite from a number of deposits range from 1600 – 1500 Ma (Cumming and Krstic, 1992; Fayek et al., 2002; Alexander et al., 2003) and 1460 – 1350 Ma (McGill et al. 1993; Fayek et al. 2002; McArthur River, Cigar Lake, and Sue deposits). For example, Carl et al. (1992) found the oldest mineralization to be  $1421 \pm 49$  Ma (U/Pb) with subsequent remobilization at 1215 Ma (Sm/Nd). Höhndorf (1985) documented three ages for Key Lake ore: 1250, 900 and 300 Ma (U-Pb & Pb-Pb discordia).

The Athabasca Group sandstones were locally silicified during a pre-ore quartz overgrowth event (Hiatt and Kyser, 2007). Diagenetic fluids (ca. 200 °C; Pagel, 1975) altered the kaolinite, montmorillonite, chlorite and low-Mg-Fe illite sandstone matrix to dominantly dickite (background alteration), with minor illite and chlorite (Quirt and Wasyluk, 1997; Earle et al., 1999; Quirt, 2001; Wasyluk, 2002; Jefferson et al., 2007). Dissolution of detrital feldspar and mica may have provided K to form illite from kaolinite (Hoeve and Quirt, 1984).

## SAMPLING FOR THIS STUDY

This project commenced in August 2012, with examination and sampling of drill-core from along the P2 structure (exploration holes beginning with MC) and within the McArthur River underground mine (underground collared drill-holes are denoted H or MO) (Fig. 1). Most samples collected are basement metapelite and pegmatite. However, seven samples of sandstone close to the unconformity were also collected. Two barren drill-holes that did not intersect the P2 fault (MC344 and MC385), two barren holes that did intersect the P2 fault (MC361 and MC362), and two weakly mineralized holes that intersect the P2 fault outside of the mine area (MC370 and MC349) were sampled. Drill-holes MC344 and MC385 intersected the hanging-wall and footwall of the P2 fault, respectively. Drill-hole MC370 intersected the P2 fault where it comprises two structural slices of the unconformity between the Athabasca Group and basement (Fig. 1C). MC349, MC361 and MC362 transected the P2 fault zone strictly in the basement. Drill-hole MC349 (EOH 665 m) intersected the basement in both the P2 fault zone and footwall. Drill-hole MC361 (EOH 654.5 m) intersected the P2 fault zone at the unconformity (at a depth of ~500 m downhole) from the basement hanging-wall and into the footwall. Low-grade disseminated uraninite is perched in the Athabasca sandstone within the P2 fault zone proximal to MC349 and MC370.

Nine drill-holes from the McArthur River mine were also sampled: two from Zone 1 (H3559 and H3576), six from Zone 2 (MO227, H201, H203, H231, H347, and H493), and one from Zone 3 (H729). The sampled Zone 2 drill-holes were from three sections (10 m window width): H231 and MO227 were from section 8180 W, H203 was from 8240 W, and H201, H347 and H493 were from section 8273 W (Fig. 1D). Drill-holes H201, H347 and H493 from the Zone 2 underground mine intersected the basement rocks where the P2 fault zone is in contact with the basement hanging-wall and middle wedge. Drill-hole H729 was collared in the underground mine of Zone 3 where it first intersected the basement hanging-wall, then the P2 fault zone, middle block and quartzite footwall. The total of 159 drill-core samples collectively represent characteristic features such as the least altered rocks, Green Zone, Red Zone, Bleached Zone, and Zone 2 breccia.

## METHODOLOGY

After careful examination of drill-core samples, representative samples were selected for polished thin-sections (89 in total). Minerals were identified using short-wave infrared spectroscopy (SWIR) on clean drill-core samples, using a TerraSpec 4 Hi-Res Mineral Spectrometer with collection time of at least 5 seconds to ensure the reproducibility of spectra. The software SpecMIN and SpecWin were used to resolve spectra, and identify alteration minerals. Mineral spectra were also compared to Athabasca standard clays (Percival, pers. comm.) and the spectra for Athabasca clay minerals presented by Zhang et al. (2001) and Percival et al. (in press).

Petrography was described first for hand-specimens, then for selected thin-sections using plane-polarized (PPL) and cross-polarized (XPL) transmitted microscopy. Detailed textures were analyzed by a JEOL 6610LV scanning electron microscope (SEM; University of Ottawa) on carbon-coated polished thin-sections. Energy-dispersive spectroscopy (EDS) was used to semi-quantitatively analyze mineral compositions using a spectrum acquisition time of 40 seconds, a working distance of 10 mm and an accelerating voltage of 20 kV.

Quantitative analyses of biotite, garnet, illite, chlorite, kaolinite and tourmaline for major and minor constituents ( $\text{SiO}_2$ ,  $\text{TiO}_2$ ,  $\text{Al}_2\text{O}_3$ ,  $\text{FeO}$ ,  $\text{MnO}$ ,  $\text{ZnO}$ ,  $\text{MgO}$ ,  $\text{CaO}$ ,  $\text{Na}_2\text{O}$ ,  $\text{K}_2\text{O}$ ,  $\text{Cl}$ ,  $\text{BaO}$ ,  $\text{F}$  and  $\text{SrO}$ ) were obtained at the University of Ottawa using a JEOL 8230 electron-probe microanalyzer (EMPA) at an

accelerating voltage of 15 kV, a beam current of 20 nA and a focused beam (10s on peak and 10s off peak counting times). The focused beam size was 5–10  $\mu\text{m}$  depending on grain size to ensure a representative average composition. The standards used are as follows: sanidine ( $\text{SiO}_2$ ), rutile ( $\text{TiO}_2$ ), sanidine ( $\text{Al}_2\text{O}_3$ ), hematite ( $\text{FeO}$ ), tephroite ( $\text{MnO}$ ), sphalerite ( $\text{ZnO}$ ), diopside ( $\text{MgO}$  and  $\text{CaO}$ ), albite ( $\text{Na}_2\text{O}$ ), sanidine ( $\text{K}_2\text{O}$ ), tugtupite ( $\text{Cl}$ ), barite ( $\text{BaO}$ ), fluorite ( $\text{F}$ ) and celestine ( $\text{SrO}$ ). Each grain was analyzed 5–7 times to ensure precision.

## RESULTS

### *Lithology of least-altered rocks*

The least-altered samples were collected at least 100 m below the unconformity at the base of background drill-hole MC344. The metapelite (Fig. 2E1) and pegmatite are mineralogically similar, both being dominated by quartz and biotite, with illitized feldspar, chloritized cordierite, garnet and minor graphite (Fig. 2E). Cordierite and graphite were found only in metapelite samples. The highest concentrations of graphite were found in samples from within the P2 fault zone. Metapelite shows weak to very strong foliation that is defined by the orientation of elongated quartz, biotite, garnet and cordierite (Fig. 2E). Biotite laths are 0.5 – 1mm long, some are partially chloritized by Fe-Mg chlorite and many also occur as ubiquitous, oval 50–100  $\mu\text{m}$  inclusions in quartz. Quartz forms coarse (> 1 mm), anhedral grains and smaller (50–100  $\mu\text{m}$ ) inclusions within coarse subhedral garnet grains (1 - 3 mm). K-feldspar grains vary in length from 0.5 – 2 mm in metapelite to > 1 cm in pegmatite, and are illitized along twinning planes and fractures. Illite occurs as fine-grained (< 2  $\mu\text{m}$ ) radiating needles. Cordierite is pseudomorphically replaced by randomly oriented, fine-grained (<2  $\mu\text{m}$ ) sudoite needles. The sudoite that replaced cordierite is partly illitized along fractures and grain boundaries (see BSE images, Fig. 2D3).

### *Alteration petrography and textural relationships*

## SWIR

Representative spectra of samples and Athabasca clay standards (Percival, written Comm.; Percival et al., in press) are shown in Figure 2. Reflective spectroscopy of most drill-core samples produced spectra characteristic of sudoite and illite (Fig. 3; spectra C & D), where the sudoite spectrum has diagnostic absorption peaks at 1400, 2190, 2250 and 2340 nm, and that of illite has sharp peaks at 1400 and 2200 nm. Absorption peaks ranging from 2100 to 2500 nm were obtained from brecciated metapelite (560.2 m) and sandstone (543 m, Fig. 3A) from drill-hole MC370 where the P2 fault offsets the unconformity. These peaks are considered to be characteristic of magnesiofoitite (Zhang et al., 2001, Percival, written Comm.; Percival et al., in press). Double peaks at ca. 1400 and 2200  $\mu\text{m}$  were observed from basal quartzite (499.4 m; Fig.3B) immediately below the unconformity in drill-hole MC344 and hematitized metapelite (686 m) in the footwall to the P2 from drill-hole MC385, and are interpreted to be of dickite.

### *Hanging wall & footwall alteration in metapelite and pegmatite*

The basement rocks from background drill-holes exhibit a colour profile consistent with the studies of MacDonald (1980; 1985): a Green Zone at deeper levels, a middle Red Zone, and a discontinuous Bleached Zone that extends along the unconformity. All three zones were observed in drill-hole MC344 (Fig. 1B) that intersects the P2 hanging-wall. However, only the Red Zone and Bleached Zone were recognized in drill-hole MC385 (P2 footwall), as the drill-hole terminated before entering

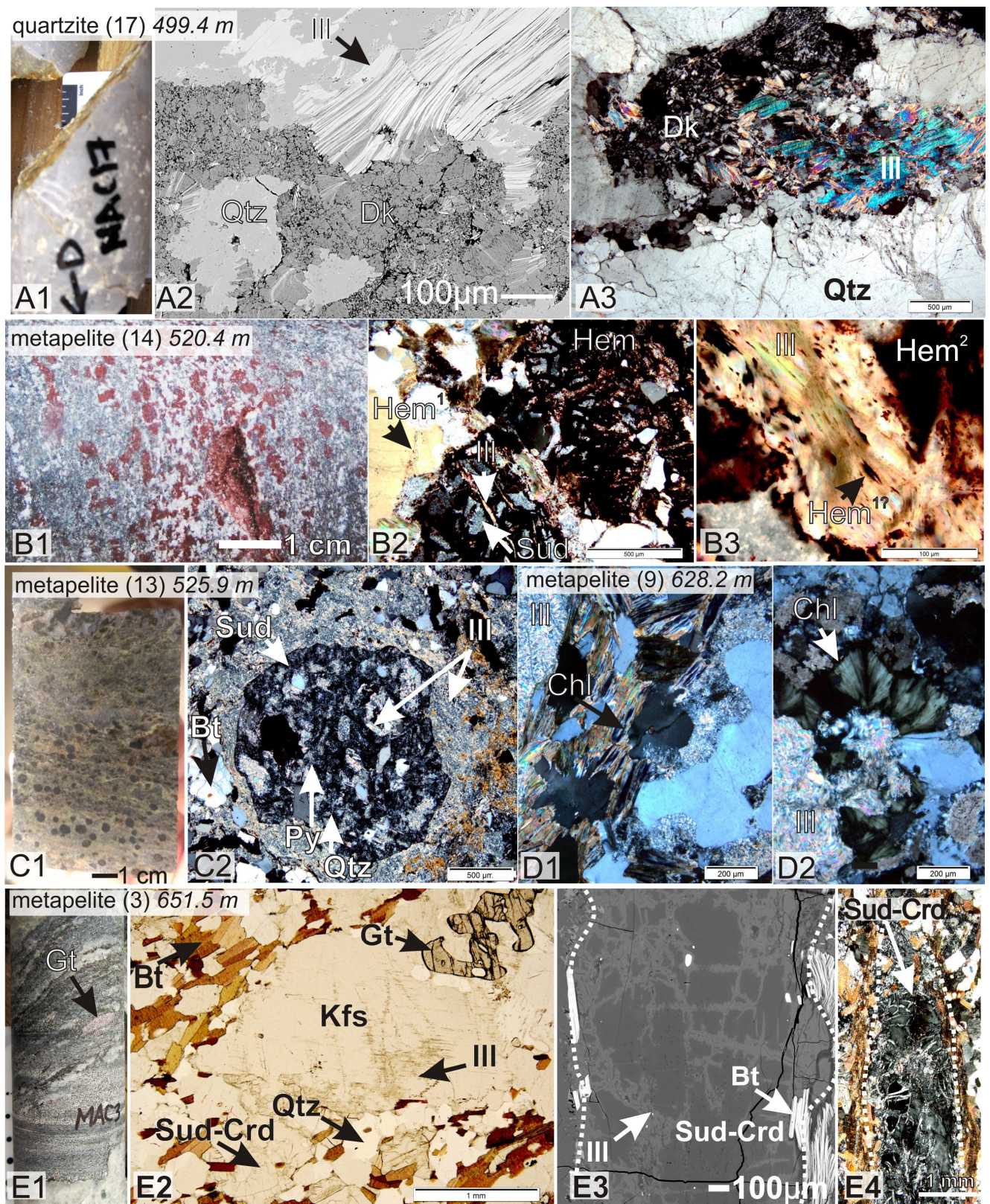


**Figure 2:** Drill-core photos, photomicrographs and BSE-images of samples from background drill-hole MC344 that intersected the basement rocks within the hanging-wall to the P2 fault. Samples are shown in order of proximity to the unconformity (~498 m) with “A” being the closest. **A1)** Drill-core sample of bleached quartzite from immediately below the unconformity. **A2)** BSE-image of fine-grained dickite “books” (Dk; dark grey) that are replaced by fine- and coarse-grained illite (Ill; light grey). **A3)** Photomicrographs (XPL) of coarse-grained illite and dickite within bleached quartzite. **B1)** Drill-core sample of hematized metapelite from the Red Zone. **B2)** Photomicrographs of the two generations of hematite: Hem<sup>1</sup> is early and trapped between annealed quartz grains and within recrystallized illite cleavages and Hem<sup>2</sup> is

later and overprints sudoite-altered garnet (Sud). The grain boundary of the relict garnet is distinguishable and the hematized garnet in the lower left corner of the image is cross-cut by a veinlet of illite. **B3**) Photomicrograph (400X; XPL) of hematite ( $\text{Hem}^{17}$ ) that was possibly trapped in cleavages of coarse-grained illite (pseudomorphic replacement of Fe-Mg chlorite). **C1**) Drill-core sample showing chloritized metapelite from the upper Green Zone. **C2**) Photomicrograph (XPL) showing garnet replaced by sudoite and that contains fine-grained illite aggregates, pyrite (Py), and inclusions of quartz (Qtz). Fine-grained illite has partially replaced sudoite and quartz. **D**) Photomicrograph (XPL) of moderately chloritized metapelite from Green Zone that shows blue chloritized biotite that is altered to high-birefringent illite. **D2**) Photomicrograph (XPL) of green radial aggregate of Fe-Mg chlorite in metapelite. **E1**) Drill-core sample of relatively unaltered and weakly foliated metapelite. **E2**) Photomicrograph (PPL) of metapelite composed of garnet (Gt), biotite (Bt), slightly illitized K-feldspar (Kfs), cordierite altered by sudoite (Sud-Crd) and quartz. **E3/E4**) BSE-image (E3) and photomicrograph (E4; XPL) of sudoite altered cordierite. The BSE-image shows that the sudoite is illitized along fractures.

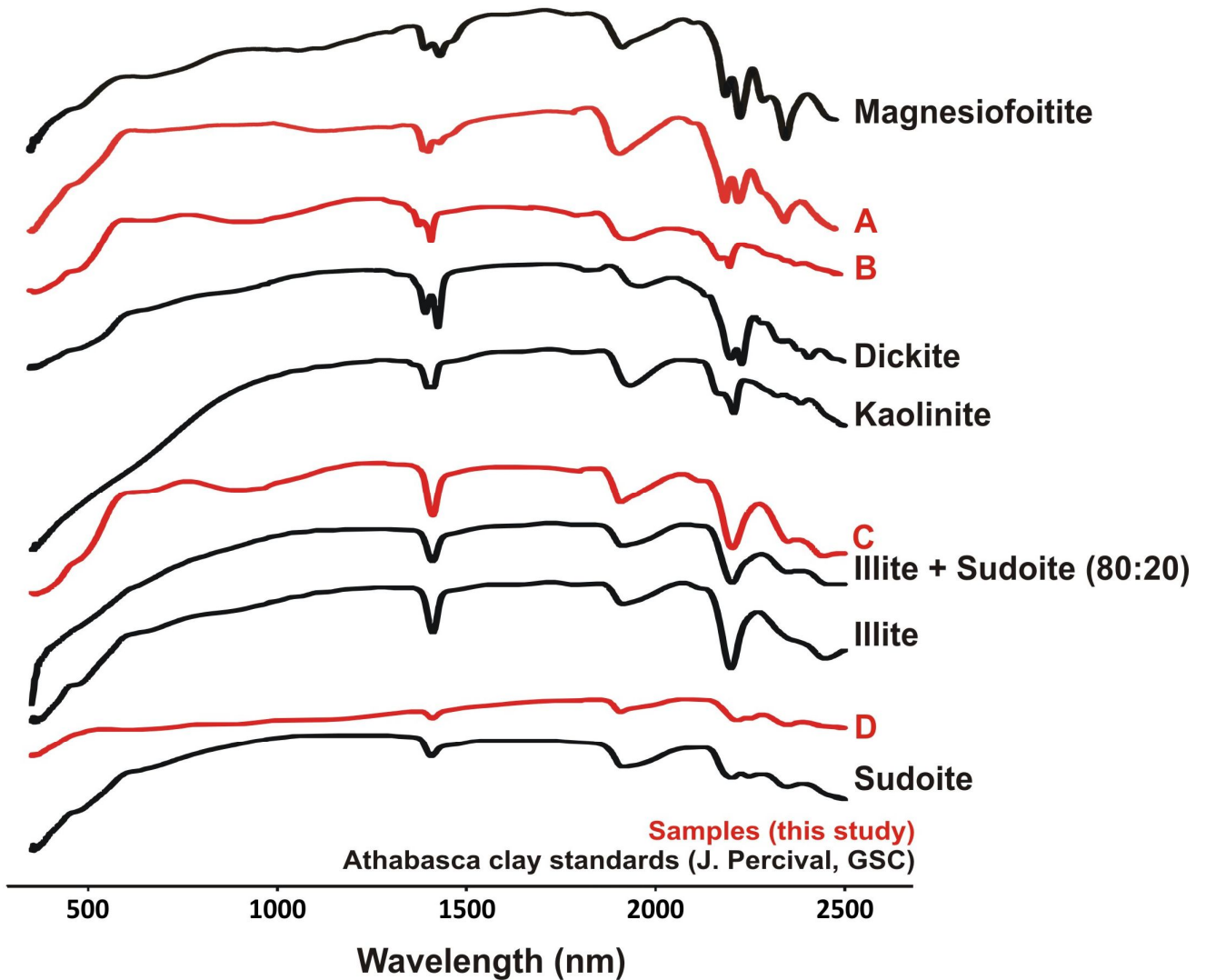


**Figure 3:** Representative infrared spectra of samples analysed in this study (red) and Athabasca clay standards (black). Spectra A is interpreted to be magnesiofoitite and was produced from blue clay altered sandstone, immediately above the unconformity within the P2 fault (MC370, 543 m). Spectrum B (MC344, 499.4 m) is interpreted to be a mixture of dickite and kaolinite (based on double peaks at 1400 and 200 nm) and is produced by samples from the Bleached Zone and Red Zone. Spectra C and D are most typical for samples and represent sudoite and illite mixtures.

the Green Zone in the footwall. Below the Green Zone in drill-hole MC344, the rocks are relatively unaltered metapelite and pegmatite.

The least altered rocks gradationally transition into the overlying Green Zone (Fig. 2C). Chlorite and illite replace mafic minerals (garnet and biotite) and feldspar (Fig. 2C2) and chlorite also forms fine-grained radial aggregates (ca. 200  $\mu\text{m}$ ; Fig. 2C3). In drill-core, the metamorphic foliation is preserved (Fig. 2C1), although dark green chlorite replaces garnet, and lighter yellow-green and white clay replaces all other material except quartz. In a thin-section of moderately chloritized metapelite, Fe-Mg chlorite forms blue-purple pseudomorphs of biotite, green veinlets that fragmented garnet and green radial aggregates along grain boundaries (Fig. 2D). Fe-Mg chlorite that replaces biotite is partially replaced by illite, as indicated in thin section by a higher birefringence in cross-polarized light (Fig. 2D1). In strongly chloritized metapelite from the Green Zone, biotite inclusions in quartz remain unaltered (Fig. 2C2) yet Fe-Mg chlorite pseudomorphs of biotite do not remain and there are no relict grains of cordierite. Sudoite completely replaced garnet and pyrite fills veinlets. Fine-grained aggregates and veinlets of illite, and grains of quartz are within the sudoite pseudomorphs of garnet (Fig. 2C2).

The Green Zone is overlain by the Red Zone (Fig. 2B, 4D & 4E), separated by a transition zone of alternating green and red alteration. The Red Zone is best preserved in drill-hole MC385 (at depths 686 m – 678.8 m) where it comprises at least two generations of hematite. Early hematite ( $\text{Hem}^1$ ) is trapped between annealed quartz grains and along cleavages in coarse-grained illite. Later hematite ( $\text{Hem}^2$ ) is pervasive and overprints sudoite-altered garnet and earlier minerals (Figs. 2B2 & B3). Red Zone samples also contain relict fractured quartz ( $\text{Qtz}^1$ ), secondary re-crystallized quartz ( $\text{Qtz}^2$ ), massive reddish fine-grained (<2  $\mu\text{m}$ ) illite, fine-grained (<2  $\mu\text{m}$ ) radial aggregate “books” of kaolin-group minerals (Fig. 4D3), and coarser-grained illite laths (20-300  $\mu\text{m}$ ; Fig. 4D2). Coarse-grained illite in the Red Zone is a pseudomorph of earlier Fe-Mg chlorite (Fig. 2B) or a product of recrystallization (Fig. 4D2). Hematite ( $\text{Hem}^2$ ) is also cross-cut by veinlets of fine-grained illite (Fig. 2B2, 4A2) and kaolinite is replaced by re-crystallized illite (Fig 4C2, -D2 & E2). Red Zone samples taken closer to the unconformity contain a higher abundance of kaolin-group minerals and illite with less hematite (Fig. 4).

Along the unconformity, the Red Zone is overprinted by buff-coloured clay in the Bleached Zone (MC385: ~678.8 – 662 m). Figure 4 shows the transition of hematite dominated alteration of the Red Zone to the white-yellow clay dominated Bleached Zone as observed in drill-core MC385. Basal quartzite from the Bleached Zone that was intersected by MC344 is dominated by red-stained quartz grains (Fig. 4B1), and contains trace amounts of fine-grained kaolin-group minerals plus coarse-grained illite laths (Figs. 4A & 4B2). Pegmatite from the Bleached Zone (Fig. 4A & 4C) that was intersected by MC385 is dominated by yellow-white clay that overprints relict hematite and quartz. In thin-section, the pegmatite is dominated by fine-grained green illite and kaolinite (Fig. 4A2). Hematite in the Bleached Zone is preserved in the rims of quartz grains (Fig 4A).

### *P2 fault rocks*

The basement rocks from the P2 fault zone intersected by drill-hole MC349 contain dravite, quartz, magnesiofoitite, hematite, illite and sudoite (Fig. 5). The dravite is euhedral-subhedral, brown and pleochroic in thin sections, coarse-grained (0.2 – 1 mm) and occurs in metapelite (Figs. 5A & B) proximal to the unconformity (~2 m). Dravite is altered to magnesiofoitite at its rim (Figs. 5A2 & 5A4) or is overprinted by rutile along grain boundaries and fractures (Fig.5B2). Magnesiofoitite forms fine-grained, spherical to radial aggregates along grain boundaries and veinlets (Figs. 5A3 & 5B5).

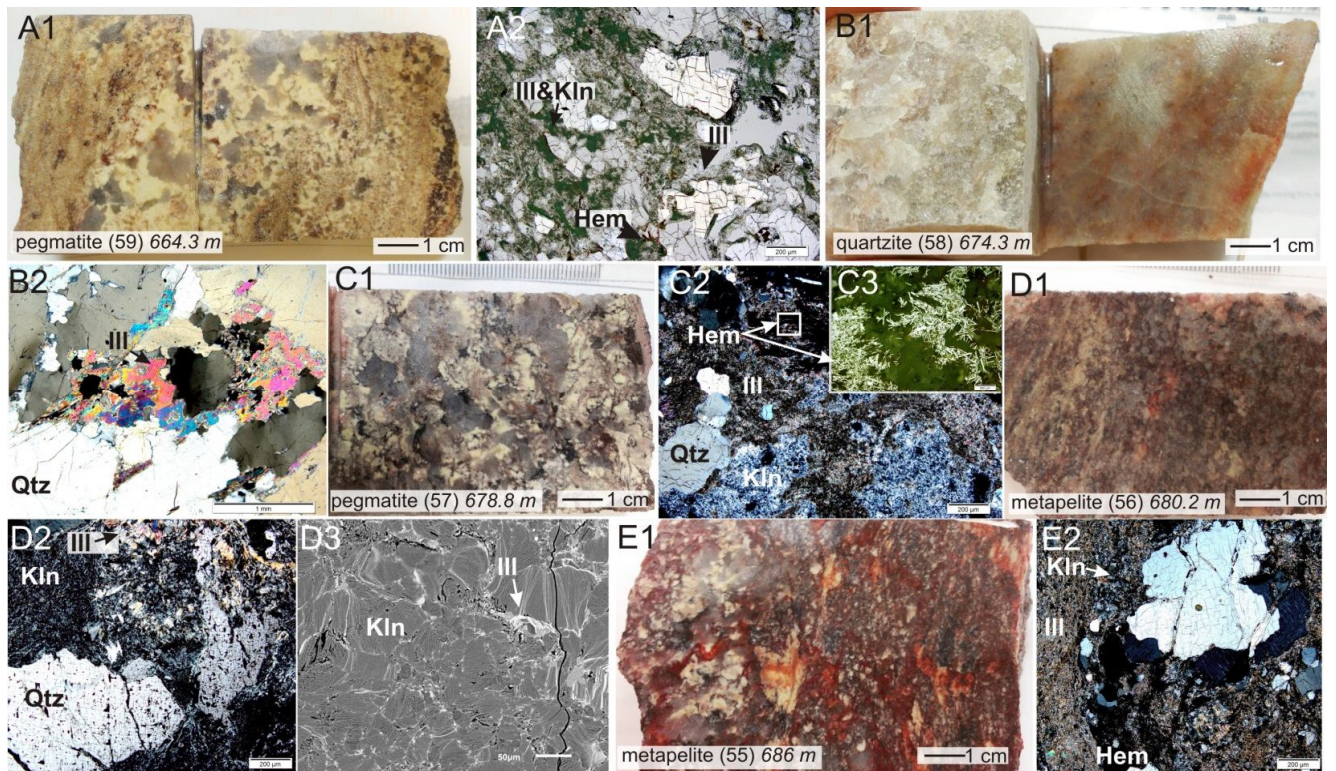


**Figure 4:** Drill-core photos, photomicrographs and BSE-images of samples that represent the Red and Bleached Zone intersected by drill-hole MC385 in the footwall to the P2 fault. Samples are shown in order of proximity to the unconformity (~498 m) with “A” being the closest. **A1)** Drill-core sample of bleached pegmatite from immediately below the unconformity. The pegmatite is altered by buff coloured clay with remnant hematite and quartz. **A2)** Photomicrograph (PPL) of relict hematite (Hem) coated quartz (Qtz) and that is surrounded by a mixture of green fine-grain illite (Ill) and a kaolin-group mineral (Kln). Recrystallized colourless coarser-grain illite is abundant and replaces finer-grained clays. **B1)** Drill-core sample of quartzite with remnant hematite staining. **B2)** Photomicrograph (XPL) of recrystallized coarse-grained illite that crystallized in a fracture in quartzite. **C1)** Drill-core sample of bleached pegmatite showing white clay that overprints hematite. **C2)** Photomicrograph of fine-grained kaolinite, fine-grained illite and brick-red hematite. Illite has a red tint. **C3)** Photomicrograph (400X; RL) of specular hematite needles. **D1)** Drill-core sample of hematized metapelite from the Red Zone. **D2)** Photomicrograph of abundant kaolinite with coarse-grained illite. Hematite occurs in fractures in quartz. **D3)** BSE-image of illite (light grey) partially replacing aggregates of kaolinite (dark grey) along grain boundaries. **E1)** Drill-core sample of hematized metapelite from the Red Zone. **E2)** Photomicrograph (XPL) of hematite, kaolinite and reddish illite.

Hematite coats quartz grains (Fig. 5B4 & C2) and invaded fine-grained sudoite and illite along microfractures (Fig. 5B3). Hematite alteration is cross-cut by magnesiofoitite veinlets (Fig. 5B5) and illite (Fig. 5B3). A single grain of monazite was noted in illite-rich pegmatite from the contact between the P2 fault zone and the footwall rocks (Fig. 5-D).

The P2 fault intersected by drill-hole MC361 (EOH 654.5 m) has an overall bleached appearance due to white and light-green clay replacements of metamorphic and secondary minerals such as hematite (Fig. 6B1). Thin-section petrography shows biotite is pseudomorphed by Fe-Mg chlorite whereas illite replaced K-feldspar (Figs. 6D & 6E). Hematite is in contact with illite (Figs. 6B2 & C). Sudoite is ubiquitous in most samples; it partially replaced fine-grained illite (Fig. 6B2), dravite (Fig. 6J1), and metamorphic garnet (Fig. 6J2). Apatite is in fine-grained sudoite immediately below the unconformity. Magnesiofoitite forms veinlets in sandstone immediately above the unconformity. Illite commonly overprints hematite (Fig. 6B2) and alters sudoite (Fig. 6F & 6J3) and biotite (Fig. 6J1). Pyrite is a common phase in late fractures. Where pyrite forms coarser (20-40  $\mu\text{m}$ ) veinlets and cubic grains, graphite is present as fine (5-10  $\mu\text{m}$ ) elongated laths.

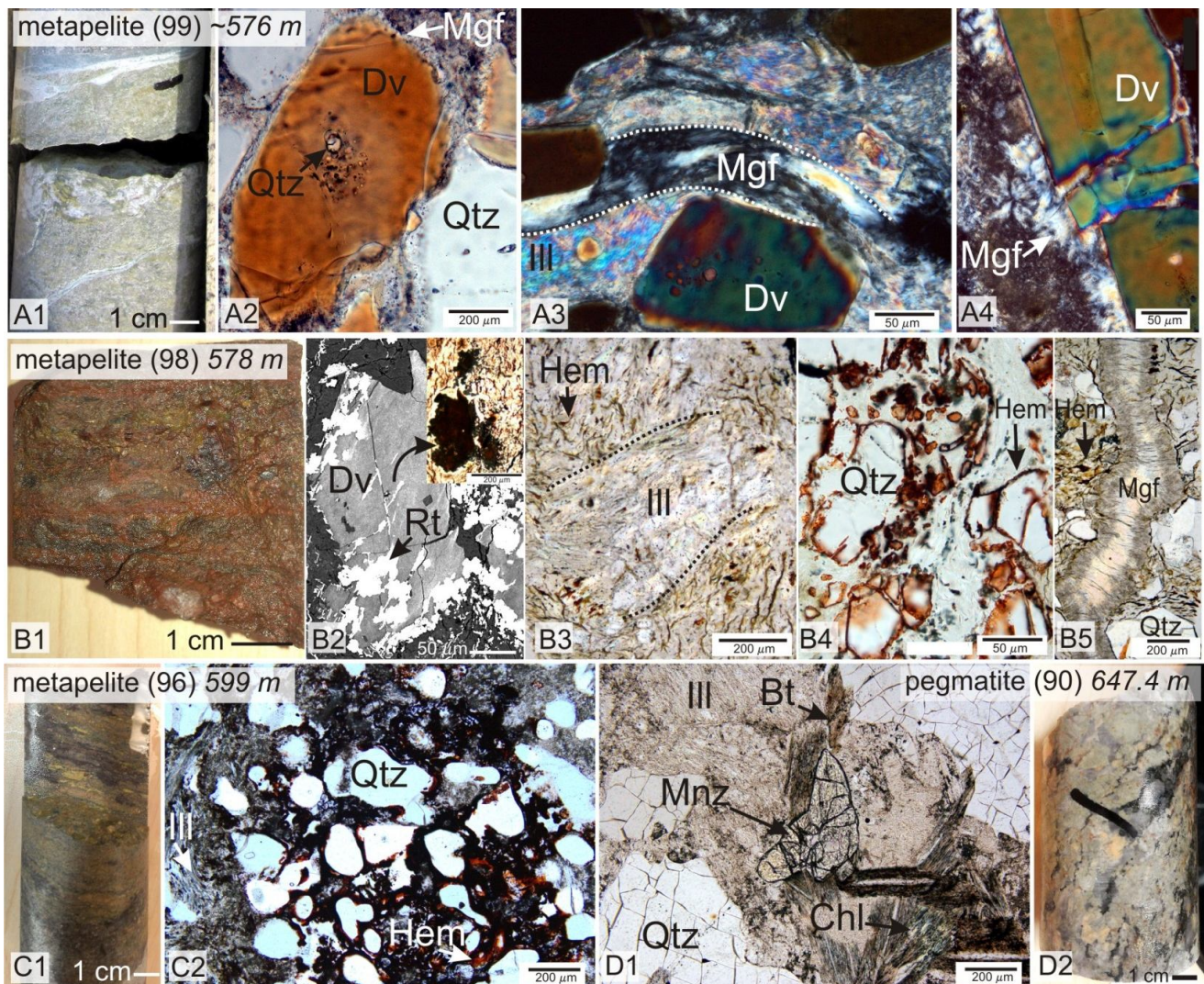


**Figure 5:** Samples from drill-hole MC349 (EOH 667) that cross-cut the P2 fault. Samples are shown in order to proximity of the unconformity (~575 m), with “A” being the closest. **A1)** Drill-core sample of tourmaline-bearing metapelite from the P2 fault. **A2)** Photomicrograph (PPL) of an euhedral grain of dravite (Dv) containing hexagonal inclusions of quartz (Qtz) and that is overgrown by fine-grained magnesiofoitite (Mgf). **A3)** Photomicrograph (XPL) of euhedral dravite bordered by fine-grained, high-birefringent, platy illite (Ill) and a veinlet of fine-grained magnesiofoitite. **A4)** Photomicrograph (XPL) of magnesiofoitite along the boundary of a dravite grain. **B1)** Fractured drill-core surface of metapelite showing brick-red to yellow-orange hematite alteration. **B2)** BSE-image and photomicrograph (top right corner; PPL) of rutile overprinting dravite and reddish-orange hematite in micro-fractures in a fine-grained illite and sudoite mixture. **B3)** Photomicrograph (PPL) showing recrystallized coarse-grained illite that cross-cuts hematite alteration. **B4)** Photomicrograph of bright red hematite coating quartz grains but not recrystallized illite. **B5)** A microphotograph showing a veinlet of magnesiofoitite that cross-cuts hematite alteration. **C1)** A drill-core sample of hematized metapelite (599 m) from the P2 fault. **C2)** Photomicrograph (PPL) showing red hematite coating quartz and fine-grained mixed chlorite-illite, and recrystallized coarse-grain illite overprinting hematite alteration. **D1)** Photomicrograph (PPL) of pegmatite that shows Ce-monazite (Mnz), surrounded by fine-grained illite, reddish-brown biotite (Bt) and chloritized biotite (Chl). **D2)** Drill-core sample showing green chlorite alteration, yellow clay and orange hematite in pegmatite.

Toward the base of drill-hole MC370 (642.7 - ~607 m), metapelite and pegmatite (Fig. 6J1) are characterized by unaltered-to-weakly chloritized biotite, and quartz, with subordinate illitized feldspar, chloritized cordierite, garnet and minor graphite (Fig. 7J2). In pegmatite, unaltered feldspar is white; illitized feldspar is green. Chlorite and illite are pervasive in altered metapelite at 606.9 m (Fig. 7I1) and metapelite and pegmatite are overprinted by hematite for ~35 m below the

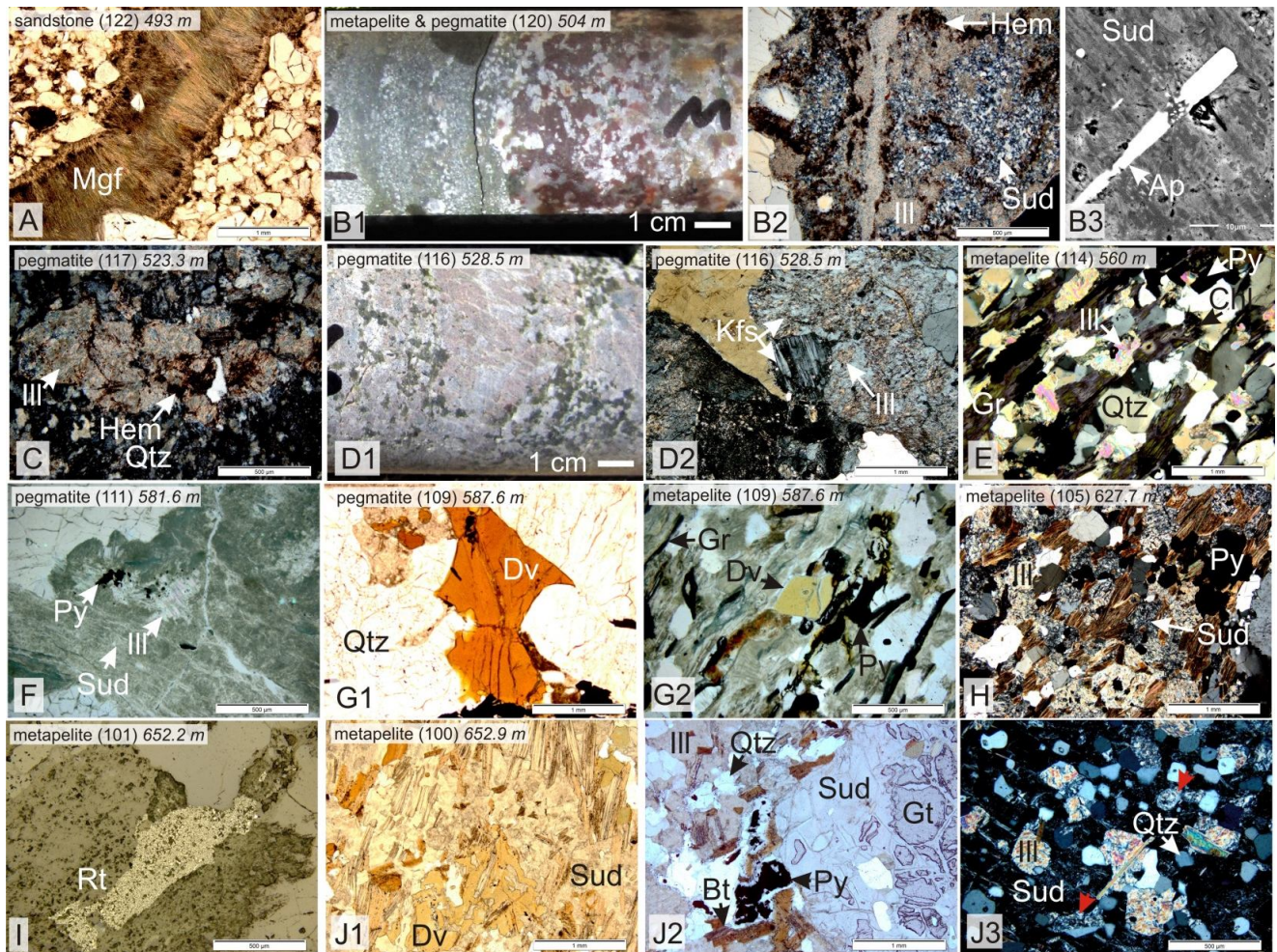


**Figure 6:** Photographs, photomicrographs and BSE-images of samples from drill-hole MC361 that intersected the P2 fault in the basement from the hanging-wall to the footwall. Sample numbers are listed in brackets beside lithology name followed by the sample depth (italicized). **A**) Veinlet of radial magnesioferrous silicate (Mgf) that cross-cuts sandstone. **B1**) Drill-core sample showing Green Zone alteration in contact with brick-red hematite. **B2**) Photomicrograph from B1 showing sudoite that partially replaced fine-grained illite (Ill) that was overprinted by hematite (Hem). A veinlet of recrystallized illite occurs down the middle of the image. **B3**) BSE-image of apatite (Ap) grains surrounded by fine-grained sudoite (Sud). **C**) Photomicrograph of fine-grained illite that partially replaced hematite and quartz (Qtz), surrounded by fine-grained sudoite and quartz. **D1**) Drill-core sample showing partially illitized K-feldspar in pegmatite. **D2**) Photomicrograph of partially illitized K-feldspar (Kfs). **E**) Photomicrograph of metapelite showing illite, Fe-Mg chlorite (Chl) included by rutile, graphite, quartz and pyrite cubes. **F**) Photomicrograph of pegmatite that contains coarse-grained illite, embayed quartz and pyrite surrounded by sudoite. **G1**) Photomicrograph (PPL) of quartz in contact with dravite. **G2**) Photomicrograph showing dravite, pyrite, quartz, fine-grained illite and graphite. **H**) Photomicrograph (XPL) of metapelite showing slightly chloritized biotite, quartz, pyrite and the replacement of sudoite by illite. **I**) Photomicrograph (RL) of illite overprinted by rutile. **J1**) Photomicrograph of metapelite with dravite replaced by sudoite and biotite replaced by illite in pegmatite. **J2**) Photomicrograph showing sudoite that replaced garnet (Gt). **J3**) Photomicrograph (XPL) showing sudoite, quartz and illite that replaced garnet. Illite has partially replaced sudoite and quartz (red arrows).

unconformity (Fig. 7FH). Fine grained hematite forms light orange-red coatings on fine-grained illite and chlorite (Fig. 7I2) and deep red-brown micro-veinlets (Fig. 6H4). Rocks within the hematitized zone also include abundant hematite-coated, coarse-grained illite (Fig. 7G2) and fine-grained illite (Fig. 7H2 & 7H3). The basal quartz-pebble conglomerate immediately overlying the unconformity (569 m; Fig. 7E1) is also pervasively hematitized. A wedge of basement metapelite structurally overlying the basal conglomerate is altered by chlorite and illite (Fig. 7C) and the sandstone above



**Figure 7:** Samples from drill-hole MC370 that intersected the P2 fault at the sandstone-basement interface (570.4 m). **A)** Metapelite from the P2 fault that was placed over the Athabasca Group, showing hematite alteration overprinted by pervasive illite alteration. **B1)** Drill-core sample of sandstone from between two wedges of basement rocks within the P2 fault brecciated by magnesiofoitite (Mgf) veinlets. **B2)** Photomicrograph (XPL) of a magnesiofoitite veinlet in sandstone. **C)** Drill-core sample of chloritized and illitized metapelite from the basement wedge overlying sandstone within the P2 fault. **D)** Illitized and magnesiofoitite altered metapelite from the basement wedge overlying sandstone within the P2 fault. **E1)** Drill-core sample of pervasively hematized basal quartz conglomerate. **E2)** Photomicrograph (PPL) of fine-grained green illite replaced and cross-cut by hematite blocks and veins **F)** Drill-core sample of hematized pegmatite with relict green alteration. **G1)** Drill-core sample of orange-red hematized metapelite. **G2)** Photomicrograph (XPL) of coarse-grained illite overprinted by dark red-brown hematite along cleavage planes. **H1)** Drill-core sample that shows hematized pegmatite with relict green alteration. **H2)** Photomicrograph (PPL) of illite (Ill<sub>1</sub>) overprinted by brick-red-brown hematite and veinlets of green illite (Ill<sub>2</sub>) cross-cut by orange brown hematite. **H3)** Photomicrograph (XPL) of illite rimmed by hematite along grain boundaries and cleavage planes. **H4)** Photomicrograph (400X; PPL) of illite overprinted by hematite. **I1)** A drill-core sample of green metapelite. **I2)** Photomicrograph that shows relict light orange-red hematite coated grains of illitized and chloritized feldspar, biotite, and cordierite. Pyrite occurs as fine-grained veinlets that infilled fractures (RL image upper left had corner). **J1)** Drill-core sample of relatively unaltered metapelite and pegmatite. **J2)** Photomicrograph of relatively unaltered metapelite that shows the typical metamorphic mineral assemblage of the basement metapelite.

the basement wedge (543 m) is cross-cut by blue veinlets of magnesiofoitite (Fig. 7B). A second wedge of metapelite overlying the sandstone is pervasively altered to illite and hematite (Fig. 7A). Two samples of graphitic metapelite from the middle block (a structural repetition of the unconformity sequence between the footwall and hanging-wall) of the P2 fault zone were obtained from drill-hole H3559. Dravite fills veinlets along the foliation (Fig. 8A & 8C) and contains numerous quartz inclusions (Fig. 8D). Coarse-grained illite coats the boundaries of embayed quartz grains (Fig. 8B), and altered Fe-Mg chlorite laths (biotite pseudomorphs). Magnesiofoitite forms spherical or radiating fine-grained aggregates, pseudomorphs of dravite and these are rimmed by graphite (Fig. 8E).

The metapelite and pegmatite from drill-holes H201, H347 and H493 (Zone 2 underground mine; Fig. 1D) are extensively altered to greenish-yellow clay (Fig. 9-G1), and brecciated by green and white-blue veinlets (Fig. 9F1). Coarse tourmaline grains are schorl at their core and dravite at their rim (Fig.

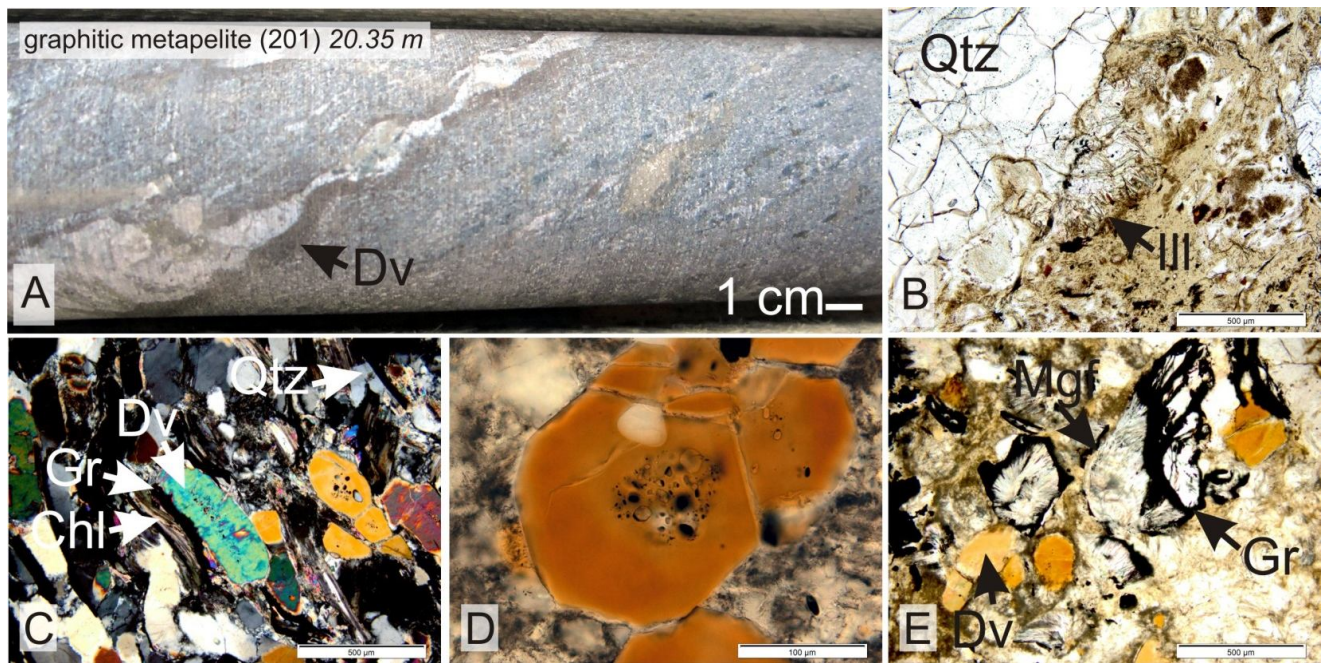


**Figure 8:** Graphitic metapelite intersected by drill-hole H3559 in the middle block within the P2 fault from Zone 1 of the underground McArthur River Mine. **A)** Drill-core photo of dravite veins within metapelite. **B)** Photomicrograph (PPL) of embayed quartz rimmed by coarse-grained illite in metapelite. **C)** Photomicrograph (XPL) of the dravite vein in A showing oriented dravite, illitized Fe-Mg chlorite and graphite. **D)** Photomicrograph (PPL) of a grain of dravite that contains many relict quartz inclusions and is bounded by fine-grained magnesiofoitite. **E)** Photomicrograph (PPL) of magnesiofoitite pseudomorphs of dravite, rimmed by early graphite.

9G2) and are replaced by sudoite along grain boundaries. Fe-Mg chlorite and sudoite co-exist (Fig. 9A): sudoite as fine-grained needles with platy fine-grained quartz (Figs. 9A1, -A2 & -E3), and Fe-Mg chlorite as coarse-grained aggregates that are replaced by sudoite (Figs. 9A1 & A2) or as veinlets that cross-cut fine-grained sudoite (Fig. 9F3). Magnesiofoitite replaces quartz (Figs. 9B, -D, and -E3) and an unidentified brown glassy mineral that has the composition of chlorite (Fig. 9F1). Pyrite forms isolated grains or veinlets along grain boundaries of magnesiofoitite (Fig. 9G1) and is replaced by sudoite (Fig. 9C).

Drill core samples from drill-hole H203 have a pervasively bleached appearance due to abundant yellow-white clay (Fig. 10C1). Thin-section petrography illustrates that illite replaced dravite (Fig. 10B2), Fe-Mg chlorite (Figs. 10A & -B3), and sudoite (Fig. 10A). Magnesiofoitite replaced illite (Fig. 10C3) and quartz (Fig. 10C4), and contains graphite along cleavage planes (Fig. 10C5). Late pyrite fills fractures in illite (Fig. 10A, -B1, & -B3).

Microphotographs of samples intersected by drill-hole H729 are in Figure 11. Metamorphic biotite (foliation evident) is replaced by Fe-Mg chlorite and fine-grained illite (Fig. 11A). Fe-Mg chlorite fills pore-spaces and was illitized (Fig. 11A). Quartz is replaced by dravite (Fig. 10B2) and magnesiofoitite (Fig. 11D). Pyrite is a late phase, and forms cubic grains and fine-grained veinlets that filled fractures in illite and fine-grained sudoite. Pyrite has a reddish tint in transmitted light, likely a result of late limonite (Figs. 11B1, B2- & -C1). Kaolinite is in pegmatite close to the VQ fault, between the middle block and footwall quartzite. BSE imaging (Fig. 11F2) shows that illite overprints kaolinite. Corundum partly replaces fine-grained kaolinite within a fracture in the quartzite footwall (Fig. 11G), here interpreted as evidence for desilicification.

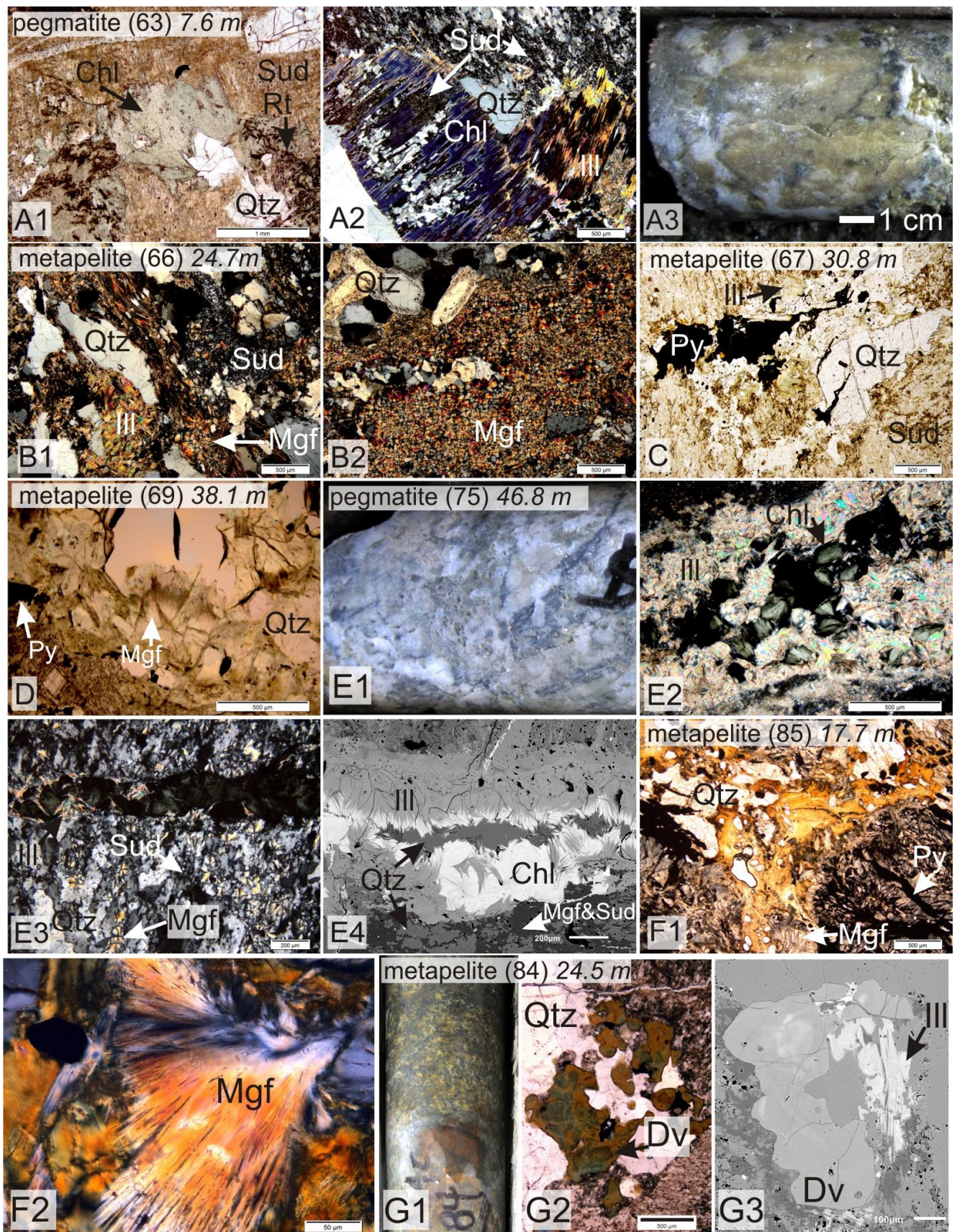


**Figure 9:** Photographs of drill-core and photomicrographs of samples from basement rocks along the P2 fault proximal to the Zone 2 ore body. A-D are metapelites intersected by H201 over ~ 30 m, E1-4 are from metapelite intersected by H347, and F-G are from pegmatite and metapelite intersected by H493. **A1)** Photomicrograph (PPL) of Fe-Mg chlorite (Chl) included by rutile (Rt) needles and partially replaced by fine-grained sudoite (Sud). Sudoite occurs as fine-grained blue-

grey clay with platy quartz. **A2)** Photomicrograph of Fe-Mg chlorite partially replaced by high-birefringent illite (Ill) and fine-grained low birefringent sudoite. Quartz (Qtz) was also partially replaced by sudoite. **A3)** Photograph of pegmatite in drill-core showing yellow-green pervasive alteration. **B1)** Photomicrograph of coarse-grained illite, fine-grained magnesiofoitite, and fine-grained sudoite in metapelite. **B2)** Photomicrograph showing pervasive magnesiofoitite alteration. The rims of the larger quartz grains in the upper left hand corner of the photo shows disequilibrium textures. **C)** Photomicrograph showing coarse-grained illite and fine-grained sudoite that partially replaced quartz. Pyrite was late and infilled a fracture. **D)** Photomicrograph showing magnesiofoitite that partially replaced quartz. **E1)** Metapelite in drill-core brecciated by chlorite and illite veinlets. **E2-4)** Veinlet of Fe-Mg chlorite that cross-cut fine-grained sudoite and replaced quartz (fine-grained plates) and magnesiofoitite. Fe-Mg chlorite is partially replaced by coarse-grained illite. **F1)** Photomicrograph of metapelite containing brown chlorite replaced by magnesiofoitite. Pyrite was late and infilled cleavage planes in magnesiofoitite. **F2)** Photomicrograph (400X; PL) showing magnesiofoitite replacement of chlorite. **G1)** Metapelite and pegmatite in drill-core altered by yellow-white clay. **G2-3)** Photomicrograph and BSE-image showing dravite (Dv) that partially replaced quartz and altered an earlier green tourmaline in pegmatite. SEM-EDS analysis shows that the altered green tourmaline has a greater wt% FeO than the brown dravite and was probably schorl.

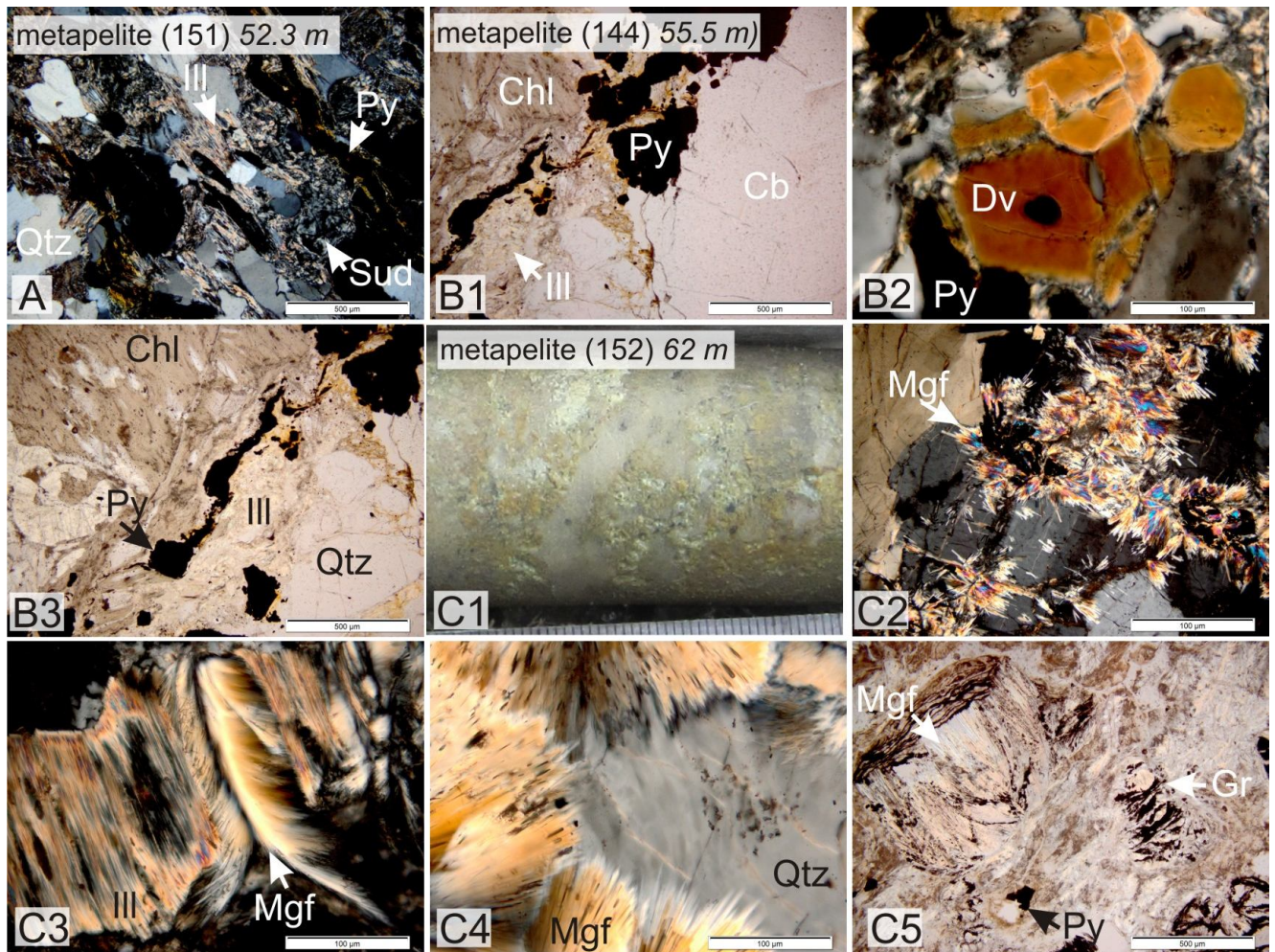


**Figure 10:** Drill-core and thin-section photos of samples from drill-hole H203 (Zone 2 underground). **A)** Photomicrograph of metapelite showing illite that replaced sudoite and Fe-Mg chlorite, and pyrite veinlets. **B1)** Photomicrograph of metapelite showing a large carbonate grain, pyrite cubes that infilled a fracture, and illite replacement of Fe-Mg chlorite. **B2)** Photomicrograph of dravite that is partially replaced by illite and pyrite. **B3)** Photomicrograph showing pyrite cubes that infilled a fracture and the replacement of chlorite by illite. **C1)** Drill-core sample of metapelite showing yellow-white pervasive clay alteration. **C2)** Photomicrograph (XPL) showing magnesiofoitite replacement of quartz. **C3)** Photomicrograph (400X; XPL) showing magnesiofoitite replacement of illite. **C4)** Photomicrograph (400X; PPL) showing magnesiofoitite that replaced quartz. **C5)** Photomicrograph (PPL) showing magnesiofoitite that replaced illite. Graphite occurs along cleavage planes and grain boundaries.

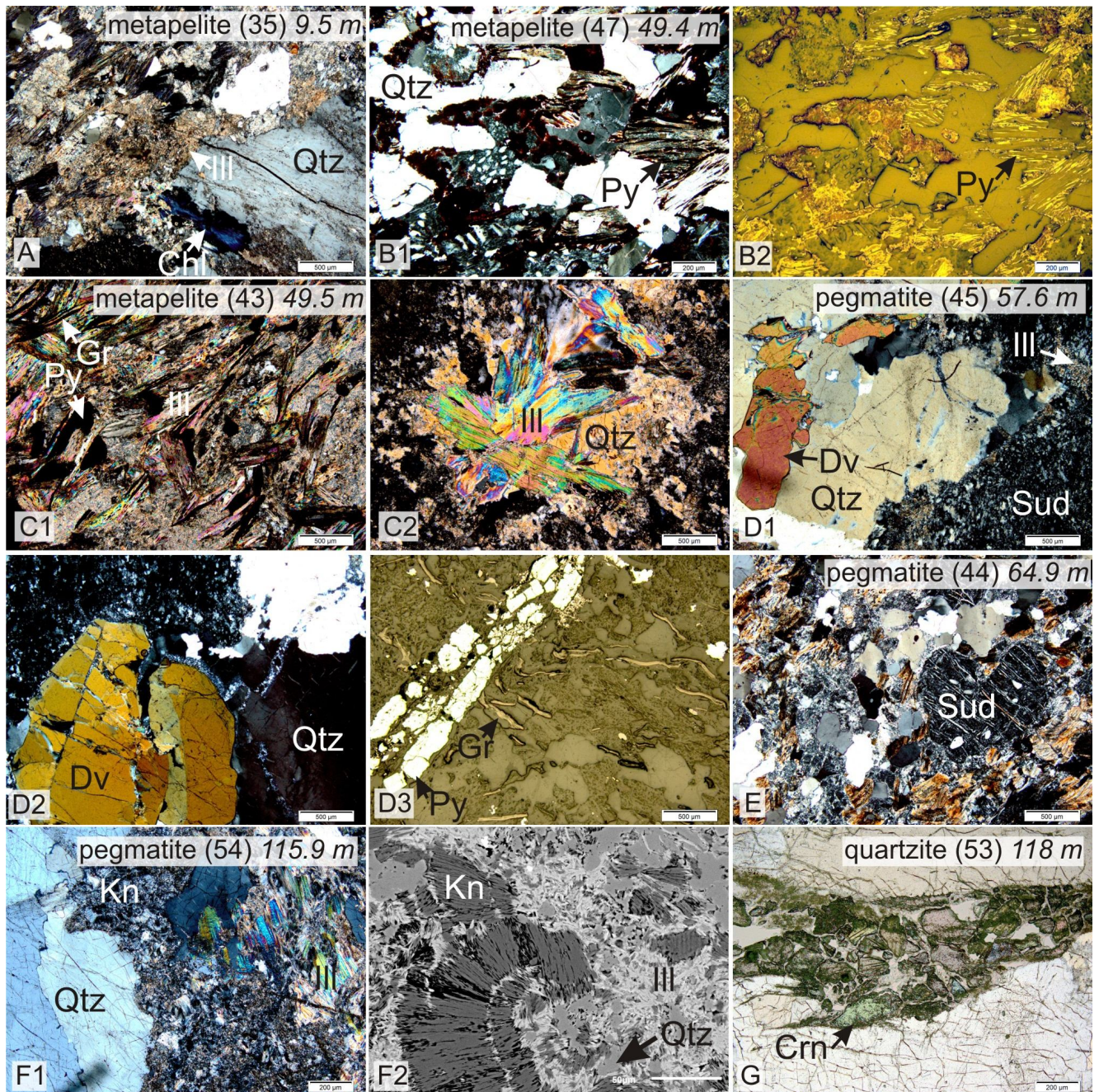


**Figure 11:** Photomicrograph of rocks intersected by drill-hole H729 (Zone 3 underground mine collared drill-hole). Samples are shown in order progressing from the hanging-wall to the P2, into middle block of the P2 fault, and in the quartzite footwall. **A)** Metapelite from the footwall to the P2 fault containing fine-grained Fe-Me chlorite aggregates (Chl) and as replacement of biotite. Fine-grained illite (Ill) partially replaced quartz (Qtz) and the Fe-Mg chlorite. **B1 & B2)** Metapelite from the middle block in the P2 fault shown in cross-polarized (B1) and reflected light (B2) showing pyrite (Py) replacement of hematite that infilled cleavages in illite and rimmed quartz grains. Remnant quartz grains that occur in fine-grained illite are evidence for quartz dissolution. **C1)** Pyrite and graphite (Gr) infilled cleavage planes in coarse-grained illite pseudomorphs of Fe-Mg chlorite. **C2)** Coarse-grained illite partially replaced quartz in metapelite. **D1 & D2)** Quartz replaced by dravite in pegmatite from the middle block in the P2 fault. Quartz, fine-grained illite, and dravite are partially replaced by sudoite (Sud). **D3)** A late pyrite vein that cross-cut graphite laths. **E)** Sudoite replaced fine-grained illite, biotite and cordierite in pegmatite. **F1)** Photomicrograph showing coarse-grained illite replaced quartz and kaolinite (Kn) partially replaced the illite. **F2)** BSE-image showing illite (light grey) that overprinted kaolinite (dark grey). **G)** Crystalline corundum (Crn) that partially replaced kaolinite and quartz in a veinlet in quartzite.

## Mineral chemistry

All data tables are located in the Appendix. Representative analyses of metamorphic biotite and garnet from metapelite in drill-hole MC344 are presented in Table 1. Biotite is intermediate composition ( $X_{\text{Fe}} = \sim 0.50$  where  $[X_{\text{Fe}} = \text{Fe}/(\text{Fe}+\text{Mg})]$ ) between annite and phlogopite end-members. Garnet is Fe-rich almandine ( $X_{\text{Fe}} = 0.83$ ) and contains low MnO (2.09 wt. %) and CaO (0.96 wt.%). K-feldspar composition, which was semi-quantitatively determined using SEM-EDS, is almost pure orthoclase ( $\text{K}_2\text{O} = \sim 15$  wt.%;  $\text{Na}_2\text{O} = \sim 1$  wt.%).

EMPA and SEM-EDS data for chlorite are in Table 2. Iron is assumed to be Fe(II) in all minerals. Sudoite and Fe-Mg chlorite were identified based on Al, Fe and Mg at the octahedral site (Fig. 12). Sudoite has three main compositions, those replacing cordierite and garnet, and that which forms a fine-grained matrix in altered metapelite. Sudoite that replaces cordierite has an average chemical formula of  $(\text{Mg}_{1.14}\text{Fe}_{0.61}\text{Al}_{2.86})(\text{Si}_{3.6}\text{Al}_{0.4})\text{O}_{10}(\text{OH}_{7.78}\text{F}_{0.22})$ , whereas sudoite that replaces garnet is more Mg-rich with an average chemical formula of  $(\text{Mg}_{1.67}\text{Fe}_{0.19}\text{Al}_{2.9})(\text{Si}_{3.45}\text{Al}_{0.55})\text{O}_{10}(\text{OH}_8)$ . In altered metapelite Fe-Mg chlorite replaces biotite, forms fine grained aggregates and has an average chemical formula of  $(\text{Mg}_{2.14}\text{Fe}_{1.97}\text{Al}_{0.56})(\text{Si}_{2.90}\text{Al}_{2.10})\text{O}_{10}(\text{OH}_{7.96}\text{F}_{0.04})$ .

Chemical data from EMPA analysis of kaolinite, fine-grained and coarse-grained illite from background hole MC344 are in Table 3. Kaolinite has an average mineral formula of  $\text{Al}_{1.91}\text{Si}_{2.03}\text{O}_5(\text{OH})_4$ . Fine-grained illite from metapelite sampled in drill-hole MC344 has a mineral formula of  $\text{K}_{1.63}(\text{Mg}_{0.34}\text{Fe}_{0.21}\text{Al}_{3.59})(\text{Al}_{1.54}\text{Si}_{6.46})\text{O}_{20}(\text{OH})_4$ . Coarse-grained illite contains slightly less MgO on average, with an average mineral formula of  $\text{K}_{1.81}(\text{Mg}_{0.11}\text{Fe}_{0.10}\text{Al}_{3.82})(\text{Al}_{1.81}\text{Si}_{6.19})\text{O}_{20}(\text{OH})_4$ . EMPA data for coarse-grained illite from sandstone, metapelite and pegmatite along the P2 fault are in Table 4. Illite from pegmatite and metapelite typically contain greater MgO contents (0.40 to 9.03 wt.% MgO) whereas sandstone illite is richer in Fe (2.95 wt.%  $\text{Fe}_2\text{O}_3$ ).

EMPA data for dravite and magnesiofoitite are presented in Tables 5 and 6, respectively. Dravite calculated assuming stoichiometric boron and based on 24.5 oxygen is:  $(\square_{0.4}\text{Na}_{0.6})(\square_{0.2}\text{Mg}_{1.9}\text{Fe}_{0.5}\text{Ca}_{0.2}\text{Ti}_{0.2})(\text{Al}_{5.9}\text{Fe}_{0.1})(\text{Si}_{5.7}\text{Al}_{0.3}\text{O}_{18})(\text{BO}_3)_3(\text{OH}_{3.8}\text{F}_{0.2})$ , where  $\square$  represents site vacancies. The mineral formula of magnesiofoitite is:  $(\square_{0.75}\text{K}_{0.08}\text{Na}_{0.17})(\square_{0.23}\text{Ca}_{0.02}\text{Fe}_{0.04}\text{Mg}_{2.10}\text{Al}_{0.61})\text{Al}_6(\text{Al}_{0.22}\text{Si}_{5.78}\text{O}_{18})(\text{BO}_3)_3(\text{F}_{0.02}\text{OH}_{3.98})$ . Schorl (partially replaced by dravite) was identified in one sample from Zone 2 and its chemistry, semi-quantitatively determined using SEM-EDS, is 39.1 – 40.9 wt.%  $\text{SiO}_2$ , 0 – 1.4 wt.%  $\text{TiO}_2$ , 11 – 14 wt.% FeO, 4.6 – 6.0 wt.% MgO, 0.8 – 1.1 wt.% CaO, and 1.9 – 2.1 wt.%  $\text{Na}_2\text{O}$ .

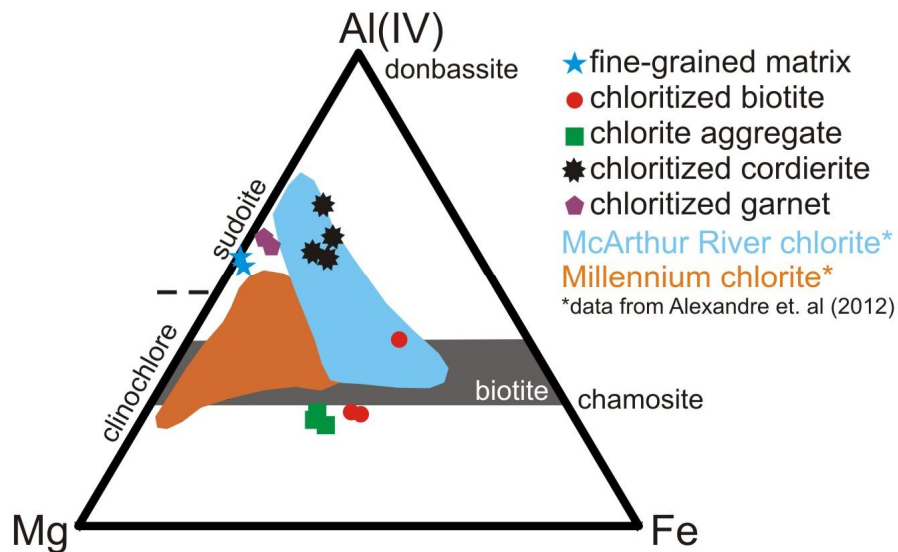


**Figure 12:** AFM diagram (Al = octahedral site Al) to classify chlorite species analyzed by EMPA and SEM. Two species of chlorite are identified: sudoite and Fe-Mg chlorite. The blue and orange fields coincide with chlorite data from Alexandre et al. (2012).

## DISCUSSION

### *The paragenesis of alteration in the basement and in the P2 fault zone*

At least two compositionally distinct generations of chlorite are in the Green Zone (Fig. 12): Fe-Mg chlorite replacing metamorphic biotite and garnet, and forming as radial aggregates, and sudoite replacing garnet and cordierite. Notably, chloritized biotite is partially illitized in the Green Zone and is completely pseudomorphed by illite in the Red Zone. In drill-hole H201, Fe-Mg chlorite is altered to fine-grained sudoite + quartz, and is also illitized. Therefore the alteration of Fe-Mg chlorite to coarse-grained illite is complete in the Red Zone, but not in the Green Zone, and the formation of sudoite post-dated formation of Fe-Mg chlorite. Fe-Mg chlorite also locally forms fine veinlets with illite that brecciate pegmatite and metapelite and may be a second, late, generation. Sudoite replaced garnet and cordierite before the latest hematization event ( $\text{Hem}^2$ ) because hematite overprints the sudoite of the

Green Zone, but after the formation of Fe-Mg chlorite because sudoite is present but Fe-Mg chlorite is absent in the most extensively altered Green Zone rocks.

Kaolinite and hematite ( $\text{Hem}^2$ ) appear to be coeval in the Red Zone as one does not replace the other and both minerals are partially replaced by late illite. An early hematite event ( $\text{Hem}^1$ ) is characterized by fine veinlets present between annealed quartz grains and along cleavages in coarse-grained illite (Fe-Mg chlorite pseudomorph). Dickite is present in some Red Zone and Bleached Zone samples based on double peaks from SWIR spectra; however the optical properties, morphologies, and textures of kaolinite and dickite are similar under microscope and it is difficult to differentiate them.

Illite is ubiquitous throughout all alteration zones in the basement. At least two generations of illite are recognized in the basement rocks: i) early illitization of feldspar, and ii) later illite that formed by recrystallization of early illite; this replaced Fe-Mg chlorite and sudoite in the Green Zone and in the least altered rocks. The second generation of illite also altered kaolin-group minerals and cross-cuts

hematite ( $\text{Hem}^2$ ) in the Red and Bleached Zones. The “illite” described in this Open File is compositionally variable and plots in the muscovite field of the Velde diagram (Fig. 15). However, the average compositions also align with illite described by previous authors (Zhang et al., 2001; Laverett et al., 2006; Alexandre et al., 2009).

Most alteration phases described in rocks from the P2 fault have the paragenetic sequence described above. The only minerals that occur along the P2 fault but are apparently absent from samples outside of the fault zone are dravite and magnesiofoitite. As summarized by Jefferson et al. (2007) after Earle and Sopuck (1989), all rocks in this study fall within a regional dravite corridor that is narrower and differs in position from the regional illite corridor. However much of the “dravite” described by the previous researchers is reinterpreted here as magnesiofoitite (alkali deficient dravite; Rosenberg and Foit, 2006). The recognition of magnesiofoitite as a main alteration that was previously interpreted in the field as dravite opens the door to new opportunities of regional mapping. Evidence for an earlier green Fe-tourmaline (schorl) was observed in the P2 fault zone in that the cores of tourmaline grains are Fe-rich and the rims are dravite in composition. The dravite is commonly replaced by illite and magnesiofoitite. Interestingly, inclusions of quartz in dravite have the same crystallographic orientation and similar degrees of fluorescence in CL-SEM (Fig. 13), suggesting that the quartz inclusions are relicts of large grains that were replaced by the tourmaline. Magnesiofoitite formed after the second illitization event, possibly coeval with pyrite.

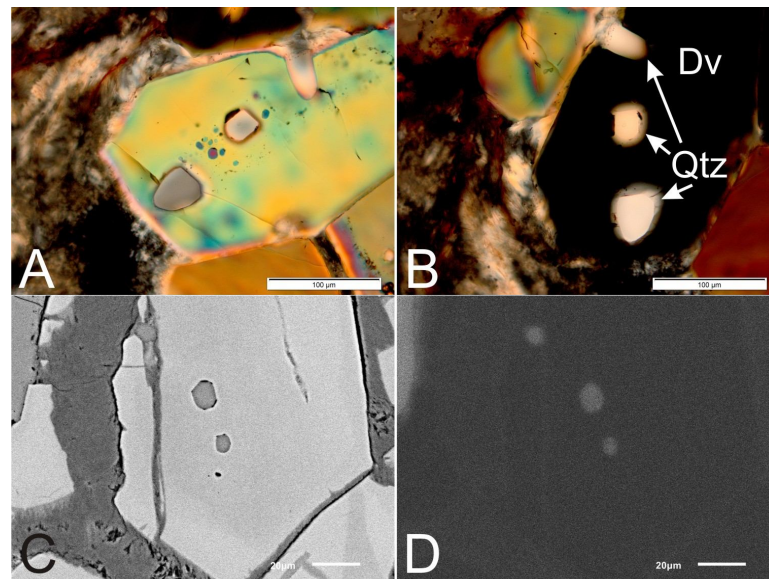


**Figure 13:** A&B) Photomicrograph (XPL) of dravite showing that quartz inclusions share the same crystallographic orientation as all inclusions are extinct (A) and transmit light (B) at the same orientation. C&D) Quartz inclusions in dravite (C) fluorescing while dravite did not (D).

The following paragenesis of alteration assemblages (Fig. 14) is listed chronologically, based on the above petrography, geochemistry, that help to reinterpret previous research:

- i) Before the earliest alteration, the basement rocks contained quartz, K-feldspar, biotite, cordierite, and garnet  $\pm$  graphite  $\pm$  pyrite  $\pm$  schorl  $\pm$  dravite;
- ii) Fine-grained illite replaced K-feldspar; Fe-Mg chlorite fragmented garnet, pseudomorphically replaced biotite (chlorite  $\pm$  rutile) and crystallized as fine-grained acicular aggregates;

- iii) Hematization (Hem<sup>1</sup>) took place before silicification (Qtz<sup>2</sup>) of Qtz<sup>1</sup>;
- iv) Sudoite (C<sup>2</sup>) replaced Fe-Mg chlorite (C<sup>1</sup>), garnet and cordierite;
- v) Hematite (Hem<sup>2</sup>) overprinted fine-grained illite, sudoite pseudomorphed garnet and cordierite, and kaolinite probably formed from the destruction of fine grained illite in the Red Zone;
- vi) An illite recrystallization event (Ill<sup>2</sup>, with minor Fe-Mg chlorite (C<sup>3</sup>)) was focused along the unconformity, but illite also forms veinlets that cross-cut hematite alteration, illite overprinted kaolinite in the Red-Zone and Bleached Zones, and illite forms veinlets and aggregates that altered sudoite and pseudomorphed Fe-Mg chlorite in the Red Zone and Green Zone in the least-altered rocks.
- vii) Magnesiofoitite altered dravite and illite, cross-cut Hem<sup>1</sup> hematite in veinlets, and possibly crystallized coeval with pyrite.

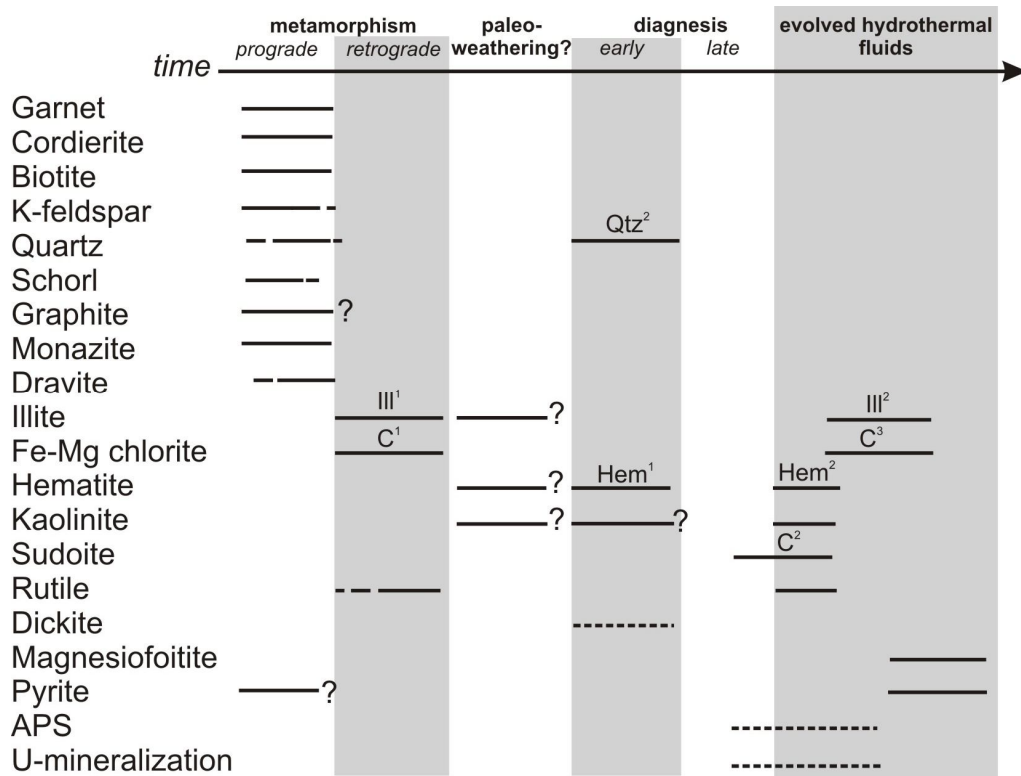


**Figure 14:** The paragenesis of alteration assemblages in the basement rocks at McArthur River. Dashed lines represent research of the Athabasca Basin rocks from Jefferson et al. (2007) and references therein.

### *The source of alteration in the basement*

All chemical data collected from illite, Fe-Mg chlorite, sudoite and biotite are presented in Figure 15 on a Velde (1984) diagram. According to Quirt (2012), Fe-Mg chlorite is a product of regional metamorphic retrogression and sudoite is an alteration product that developed during later hydrothermal activity. The textural evidence presented in this study shows that Fe-Mg chlorite and sudoite were both illitized and that Fe-Mg chlorite was replaced by sudoite. It is possible that Fe-Mg chlorite originally replaced cordierite and garnet and was subsequently replaced by sudoite. However,

cordierite is replaced by sudoite in samples where biotite and garnet are unaltered. Cordierite was preferentially chloritized prior to biotite and garnet, which is very common. The coarse-grained dravite observed in the pegmatite and metapelite along the P2 is an alteration product of earlier schorl which formed during regional metamorphism and/or is the result of B-bearing pegmatitic fluids that concentrated along the P2 fault.

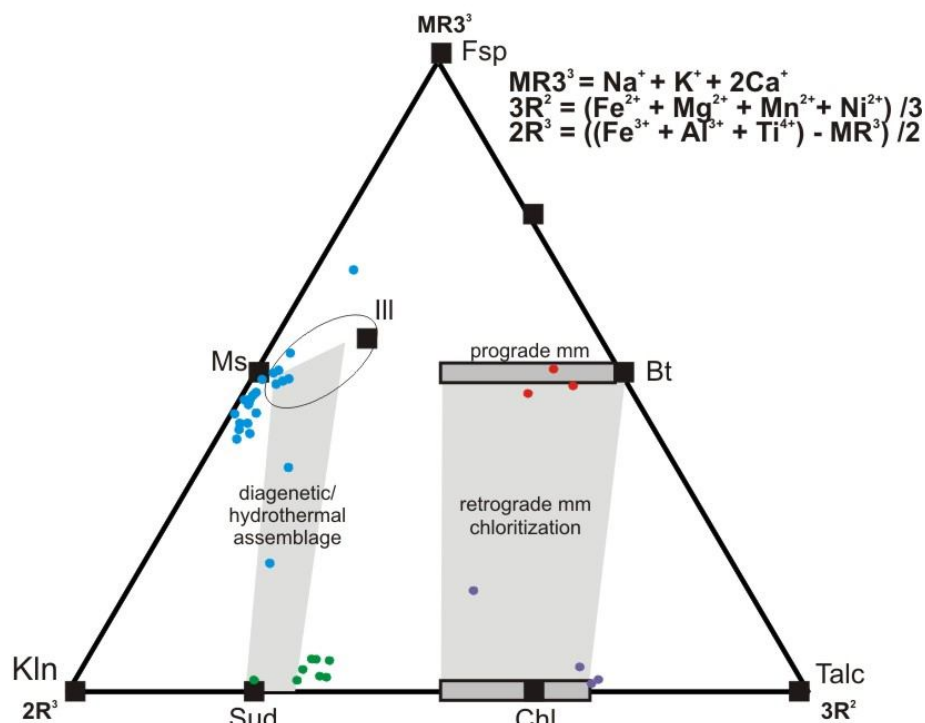


**Figure 15:** A Velde diagram (Velde, 1985) adopted from Quirt (2012) showing plotted atomic compositions of analyzed biotite (red), Fe-Mg chlorite (purple), sudoite (green) and illite (blue) from the basement rocks at McArthur River.

Macdonald (1985) attributed the Red Zone and the Green Zone to be products of weathering of the basement. This is not supported by the paragenesis of the Red Zone described above. In the Red Zone, silicates (including sudoite) are overprinted by hematite or altered to form kaolinite. Therefore, sudoite formed before the pervasive hematization in the Red Zone. It is likely that the rocks underwent multiple hematization events including paleoweathering, early diagenesis and later hydrothermal activity (post-sudoite). It was also noted in drill cores that hematitization is not restricted to the Red Zone but also extends upwards into the overlying conglomerate and sandstone units. Furthermore, in some deep drill-cores of basement rocks along the P2 (~200 m below the unconformity), wide (>10 m) zones of red hematite alteration are in contact with green alteration and bleaching that mimics the Bleached Zone, Red Zone, and Green Zone below the unconformity. Preserved hematite is also observed in basement Red Zone samples in this study. Multiple hematization events are recorded in the Athabasca Basin sandstones, with a 'primary' paleoweathering hematite, early diagenetic hematite generations preserved in overgrowths on detrital quartz grains and associated with clay development, and a late diagenetic-hydrothermal cement, Liesegang banding and discontinuous disseminations (Jefferson et al., 2007; Kyser et al., 2000; and references therein). Therefore, it is possible that the preserved hematite (Hem<sup>1</sup>) between quartz grains is a product of paleo-weathering but it is more likely evidence for early diagenetic fluids that penetrated the basement rocks, because any alteration formed during the weathering of the basement rocks would have been overprinted by a diagenetic fluid from

the overlying strata. It is probable that the pervasive hematization and kaolinite observed in the basement rocks of the Red Zone and in the Athabasca sandstones were formed by an oxidizing fluid during hydrothermal activity related to the diagenesis of the Athabasca Group and that this fluid may have been propagated along the P2 fault where it altered underlying basement rocks. It is also possible that the deeper basement hematite alteration along the P2 is due to an early diagenetic fluid.

The transition zone between the Green and Red Zones preserves fluid interactions where an oxidizing basinal fluid mixed with a reduced basement fluid. Many studies have suggested a reduced basement fluid as a reductant for uranium precipitation (Wilson and Kyser, 1987; Kotzer and Kyser, 1995; Fayek and Kyser, 1997). The evolved fluid may have been enriched in Mg, permitting alteration of Fe-Mg chlorite to sudoite.

The Bleached Zone is discontinuous along the unconformity, and lenses of bleaching also occur in the Athabasca siliciclastic rocks. The bleached appearance is caused predominately by illite and kaolin-group minerals (kaolinite ± dickite). Illite is a late phase in the Bleached Zone as it cuts kaolin-group minerals. There are several possible sources of K. The Athabasca Group sandstones contain K-feldspar and mica, and the contents of K<sub>2</sub>O exceed 5 wt.% locally (Card and Bosman, 2012). Alteration of feldspars likely released K<sub>2</sub>O to basinal fluids. The second possible source of K is pegmatite bodies in the basement which contain coarse-grained K-feldspar (1 – 2 cm).

The Athabasca Basin evolved into a hydrothermal fluid dominated system. Magnesiofoitite is a late phase in the paragenesis of the basement rocks. The basinal fluid may have evolved to crystallize magnesiofoitite, or B was locally sourced from alteration of dravite-schorl in the basement rocks. It is interesting that magnesiofoitite has been documented throughout the Read and Manitou Falls Formations of the Athabasca Group and in the basement with high concentrations along the P2 fault (Quirt, 1991; Kotzer, 1993; Rosenburg and Foit, 2006; Ng, 2012; this study).

## SUMMARY

The preliminary findings of this study suggest:

i) The alteration profile below the regional unconformity of the Athabasca Basin records the changes in fluid chemistry through fluid-rock interactions during evolution of the Athabasca basin. The Bleached Zone, Red Zone and Green Zone resulted from multiple events, including paleoweathering, diagenesis and hydrothermal alteration. An early paleoweathering profile would have been overprinted by early diagenetic fluids and these events are evidenced by hematite rims preserved by quartz overgrowths in the Red Zone, which are very similar to diagenetic hematite-quartz overgrowths in the overlying sandstone units. The pervasive hematite in the Red Zone and along the P2 is the result of an oxidizing hydrothermal fluid that propagated along faults in the area and along the unconformity and overprinted late diagenetic-hydrothermal sudoite alteration in the Green Zone from an Mg-bearing basement fluid.

ii) The overlying Athabasca Basin conglomerate and sandstone units, and the granitoid basement rocks contributed K for the formation of ubiquitous illite in the basement (in agreement with Hoeve and Quirt 1984). Illite and kaolinite are most abundant along the discontinuous Bleached Zone. The Bleached Zone and other “bleached” basement rocks are interpreted to represent rock volumes subjected to sustained fluid flow and the dissolution of hematite as the Bleached Zone overprinted the Red Zone.

iii) The P2 fault in the McArthur River area was a focus for fluid flow during the evolution of a diagenetic-hydrothermal system. Most rocks along the fault are pervasively altered to fine-grained clay minerals. Previous authors have described a regional alteration “corridor” that trends 45°N and envelopes the P2 fault. This alteration corridor, the observations that alteration is strongest along the P2 fault, and that the largest high-grade uranium ore deposit occurs along the P2, is evidence that the P2 allowed for multiple generations of basinal and hydrothermal fluids to enter the basement rocks below the Athabasca Basin.

#### ACKNOWLEDGMENTS

This is a contribution to the Targeted Geoscience Initiative Four (TGI-4) Uranium ore systems project of Natural Resources Canada and was made possible through grant funding to KH and a Research Affiliate Program (RAP) bursary to EEA. EEA also received a graduate fellowship from the Society of Economic Geologists. Expert technical assistance was received from Jeanne Percival (SWIR), Glen Poirier (SEM) and Jiri Mrazek (thin section preparation). Cameco Corporation graciously provided logistical support for the field studies and permission to publish the results.

#### REFERENCES

- Alexandre, P., Kyser, K., and Polito, P., 2003. Geochronology of the Paleoproterozoic basement-hosted unconformity-type uranium deposits in northern Saskatchewan, Canada; Uranium Geochemistry 2003, International Conference, Université Henri Poincaré, Nancy, France, April 13-16, 2003, Proceedings, p. 37-40.
- Alexandre, P., Kyser, K., and Polito, P., and Thomas, D. 2005. Alteration mineralogy and stable isotope geochemistry of Paleoproterozoic basement-hosted unconformity-type uranium deposits in the Athabasca Basin, Canada; *Economic Geology*, v. 100, p.1547–1563.
- Alexandre, P., Kyser, K., Jiricka, D., and Witt, G., 2012. Formation & Evolution of the Centennial Unconformity-Related Uranium Deposit in the South-Central Athabasca Basin, Canada; *Economic Geology* v. 107, p. 385 – 400
- Annesley, I.R., Madore, C., and Portella, P., 2005. Geology and thermotectonic evolution of the western margin of the Trans-Hudson Orogen: evidence from the eastern sub-Athabasca basement, Saskatchewan; *Canadian Journal of Earth Sciences*, v. 42, p. 573-597.
- Bronkhorst, D., Mainville, A. G., Murdock, G. M., Yesnik, L. D. 2012. McArthur River Operation Northern Saskatchewan, Canada: National Instrument 43-101 Technical Report.
- Carl, C., Pechmann, E. V., Höhndorf, A., & Ruhmann, G. 1992. Mineralogy and U/Pb, Pb/Pb, and Sm/Nd geochronology of the Key Lake uranium deposit, Athabasca Basin, Saskatchewan, Canada. *Canadian Journal of Earth Sciences*, v. 29, p. 879-895.
- Cumming, G. L., and Krstic, D., 1992. The age of unconformity-related uranium mineralization in the Athabasca Basin, northern Saskatchewan. *Canadian Journal of Earth Sciences*, v. 29, p. 1623-1639.
- Earle, S. and Sopuck, V.J., 1989. Regional litho-geochemistry of the eastern part of the Athabasca Basin uranium province, Saskatchewan, Canada; in *Uranium Resources and Geology of North America*, E. Muller-Kahle (ed.); IAEA-TECDOC-500, p. 263-296.

- Earle, S., Wheatley, K., and Wasyliuk, K., 1999. Application of reflectance spectroscopy to assessment of alteration mineralogy in the Key Lake area; MinExpo '96 Symposium - Advances in Saskatchewan geology and mineral exploration, Saskatoon, November 21-22, 1996, Proceedings, p. 109-123.
- Fayek, M., and Kyser, T.K., 1997. Characterization of multiple fluid events and rare-earth-element mobility associated with formation of unconformity-type uranium deposits in the Athabasca Basin, Saskatchewan; *Canadian Mineralogist* v. 35, p. 627-658.
- Fayek, M., Kyser, T. K., and Riciputi, L. R. 2002. U and Pb isotope analysis of uranium minerals by ion microprobe and the geochronology of the McArthur River and Sue Zone uranium deposits, Saskatchewan, Canada; *The Canadian Mineralogist*, 40, p. 1553-1570.
- Hoeve, J., and Quirt, D. H., 1984. Mineralization and Host Rock Alteration in Relation to Clay Mineral Diagenesis and Evolution of the Middle-Proterozoic, Athabasca Basin, northern Saskatchewan, Canada; Saskatchewan Research Council, SRC Technical Report 187, 187 p.
- Höhndorf, A., Lenz, H., Von Pechmann, E., Voultzidis, V., and Wendt, I., 1985. Radiometric age determinations on samples of Key Lake uranium deposits; *Geology of uranium deposits. Canadian Institute of Mining and Metallurgy Special V. 32*, p. 48-53.
- Jefferson, C.W., Thomas, D.J., Gandhi, S.S., Ramaekers, P., Delaney, G., Brisbin, D., Cutts, C., Portella, P. and Olson, R.A., 2007. Unconformity-associated uranium deposits of the Athabasca basin, Saskatchewan and Alberta; in *EXTECH IV: Geology and Uranium EXploration TECHnology of the Proterozoic Athabasca Basin, Saskatchewan and Alberta*, C.W. Jefferson and G. Delaney (eds.); Geological Survey of Canada Bulletin 588, p. 23-67.
- Kotzer, T.G. 1993. Fluid history of the Proterozoic Athabasca Basin; Ph D. thesis, University of Saskatchewan, Saskatoon, Saskatchewan.
- Kotzer, T.G., and Kyser, T.K., 1995. Petrogenesis of the Proterozoic Athabasca Basin, northern Saskatchewan, Canada, and its relation to diagenesis, hydrothermal uranium mineralization and paleohydrogeology; *Chemical Geology*, v. 120, p. 45-89.
- Kyser, K., Hiatt, E., Renac, C., Durocher, K., Holk, G., and Deckart, K., 2000. Diagenetic fluids in Paleo- and Meso-Proterozoic sedimentary basins and their implications for long protracted fluid histories; in *Fluids and Basin Evolution*, K. Kyser (ed.); Mineralogical Association of Canada Short Course Series, v. 28, p. 225-262
- Lewry, J.F., Sibbald, T., 1980. Thermotectonic evolution of the Churchill province in northern Saskatchewan; *Tectonophysics* v. 68 p.45-82
- MacDonald, C., 1980. Mineralogy and geochemistry of a Precambrian regolith in the Athabasca Basin. PhD., Dissertation. University of Saskatchewan.
- Macdonald, C., 1985. Mineralogy and geochemistry of the sub-Athabasca regolith near Wollaston Lake; *Geology of Uranium Deposits: Canadian Institute of Mining and Metallurgy Special v. 32*, p. 155-158.
- McGill, B., Marlatt, J., Matthews, R., Sopuck, V., Homeniuk, L., Hubregtse, J., 1993. The P2 North uranium deposit Saskatchewan, Canada; *Exploration Mining and Geology* v. 2, p.321- 333
- Ng, R., 2012. Geochemical and mineralogical evolution of the McArthur River Zone 4 unconformity-related uranium ore body and application of iron oxidation state in clay alteration as indicator of uranium mineralization, M.Sc. thesis, Queen's University
- Pagel, M., and Poty, B., and Sheppard, S.M.F., 1980. Contributions to some Saskatchewan uranium deposits mainly from fluid inclusions and isotopic data, in *Uranium in the Pine Creek geosyncline*, S. Ferguson and A. Goleby (eds.); Vienna, International Atomic Energy Agency, p. 639-654.

- Percival, J.B., Bosman, S.A., Potter, E.G., Ramaekers, P., Venance, K.E., Hunt, P.A., Davis, W. and Jefferson, C.W., *in press*. Hydrothermal alteration in hydro-fractured Athabasca Basin sandstone: distal expression of uranium mineralization?; *in Uranium in Canada: Geological Environments and Exploration Developments*, E.G. Potter, D. Quirt and C.W. Jefferson (eds.); *Exploration Mining and Geology* v.21.
- Quirt, D.H., 2001. Kaolinite and Dickite in the Athabasca Sandstone, Northern Saskatchewan, Canada; Saskatchewan Research Council, Publication No. 10400-16D01, p. 27
- Quirt, D.H., 2012. Clay alteration mineralogy comparisons between the Athabasca and Thelon Basins- basement alteration.; Presentation at the GEM-U workshop, St. John's, NF, May 30, 2012
- Quirt, D.H., and Wasyluk, K., 1997. Kaolinite, dickite, and other clay minerals in the Athabasca Group, Canada, and the Kombolgie Formation, Australia; 11th International Clay Conference, Ottawa, Ontario, June 1997, Proceedings, p. A61.
- Ramaekers, P., Jefferson, C.W., Yeo, G.M., Collier, B., Long, D.G.F., Drever, G., McHardy, S., Jiricka, D., Cutts, C., Wheatley, K., Catuneau, O., Bernier, S., Kupsch, B and Post, R.T., 2007. Revised geological map and stratigraphy of the Athabasca Group, Saskatchewan and Alberta; in *EXTECH IV: Geology and Uranium EXploration TEChnology of the Proterozoic Athabasca Basin, Saskatchewan and Alberta*, C.W. Jefferson and G. Delaney (eds.); Geological Survey of Canada Bulletin 588, p. 155-192.
- Rosenberg, P.E., and Foit, F.F., Jr., 2006. Magnesiofoitite from the uranium deposits of the Athabasca Basin, Saskatchewan; *The Canadian Mineralogist*, v.44, p. 959-965.
- Velde, B., 1985. *Clay Minerals: a Physico Chemical Explanation of their Occurrence*; Developments in Sedimentology No. 40. Elsevier, Amsterdam
- Wasyluk, K., 2002. Petrogenesis of the Kaolinite-Group Minerals in the eastern Athabasca Basin of northern Saskatchewan: Applications to Uranium Mineralization; M.Sc. thesis, University of Saskatchewan, Saskatoon, Saskatchewan, 140 p.
- Wilson, M.R., and Kyser, T.K., 1987. Stable isotope geochemistry of alteration associated with the Key Lake uranium deposit, Canada; *Economic Geology*, v. 82, p. 1540–1557.
- Zhang, G., Wasyluk, K., and Pan, Y., 2001. The characterization and quantitative analysis of clay minerals in the Athabasca Basin, Saskatchewan: application of short-wave infrared reflectance spectroscopy; *Canadian Mineralogist*, v. 39, p. 1347–1363.



## APPENDIX

Table 1: chemical analysis of biotite and garnet from least altered rocks from the base of drill-core MC344.

Sample (depth) lithology mineral		3 (651.5 m)				9 (628.2 m)	
		least altered metapelite			garnet	chloritized metapelite	
		biotite	biotite	biotite		garnet	garnet
		$\bar{x}$ $\sigma$	$\bar{x}$ $\sigma$	$\bar{x}$ $\sigma$	$\bar{x}$ $\sigma$	$\bar{x}$ $\sigma$	
wt%	SiO <sub>2</sub>	35.85 0.67	36.27 0.53	35.89 0.14	37.02 0.17	36.74 0.12	
	TiO <sub>2</sub>	3.66 0.65	1.30 0.80	3.90 0.16	0.01 0.01	0.00 0.00	
	Al <sub>2</sub> O <sub>3</sub>	20.41 2.24	19.51 0.51	18.99 0.18	21.45 0.09	21.26 0.07	
	FeO	18.44 2.02	16.59 1.75	19.38 0.22	33.78 0.20	34.31 0.11	
	MnO	0.04 0.01	0.04 0.01	0.04 0.02	1.32 0.04	2.86 0.07	
	ZnO	0.04 0.03	0.07 0.04	0.05 0.02	nd	nd	
	MgO	8.58 0.76	12.82 1.76	9.08 0.05	5.05 0.10	3.97 0.10	
	CaO	bdl	bdl	bdl	0.98 0.02	0.93 0.01	
	Na <sub>2</sub> O	0.10 0.02	0.24 0.12	0.09 0.01	0.02 0.01	0.02 0.01	
	K <sub>2</sub> O	8.87 1.32	9.10 0.48	9.77 0.21	0.00 0.00	0.00 0.01	
	P <sub>2</sub> O <sub>5</sub>	nd	nd	nd	0.05 0.02	0.10 0.04	
	Cl	0.06 0.01	0.04 0.02	0.07 0.00	nd	nd	
	BaO	0.03 0.02	0.06 0.03	0.06 0.03	nd	nd	
	F	0.33 0.06	0.54 0.07	0.40 0.02	nd	nd	
	Total	96.27 1.94	96.36 0.47	97.54 0.37	99.68 0.43	100.20 0.22	
	Fe/Fe+Mg	0.55	0.42	0.54	0.79	0.83	
apfu	Si	2.43	2.45	2.43	2.96	2.95	
	Ti	0.19	0.07	0.20			
	Al	1.63	1.55	1.52	2.02	2.01	
	Fe	1.05	0.94	1.10	2.26	2.31	
	Mn				0.09	0.19	
	Mg	0.87	1.29	0.92	0.60	0.48	
	Ca				0.08	0.08	
	Na	0.01	0.03	0.01			
	K	0.77	0.78	0.85			
	F	0.07	0.11	0.09			
	O*	10.00	10.00	10.00	12.00	12.00	

\*atom proportions normalized to O; SrO below detection limits (bdl); na = no data

Table 2: EMPA & SEM<sup>†</sup> analyses of chlorite in the basement rocks below the Athabasca Basin. Atoms per formula unit are normalized to O = 10.

		MC344 (background hole)												H347 (Zone 2)		H201 (Zone2)	
		3 (651.5 m) <i>relatively unaltered metapelite</i>				9 (628.2 m) <i>moderately chloritized metapelite</i>				13 (525.9 m) <i>chloritized metapelite</i>				75 (u/g) <i>altered metapelite</i>		67 (u/g) <i>altered metapelite</i>	
occurrence	chl-cordierite	chl-cordierite	chl-cordierite	chl-cordierite	chloritized bt	chloritized bt	chloritized bt	chlorite aggregate	chlorite aggregate	chloritized gt	chloritized gt	chlorite aggregate	chlorite aggregate	chlorite aggregate	fine-grained matrix		
	$\bar{x}$ $\sigma$	$\bar{x}$ $\sigma$	$\bar{x}$ $\sigma$	$\bar{x}$ $\sigma$	$\bar{x}$ $\sigma$	$\bar{x}$ $\sigma$	$\bar{x}$ $\sigma$	$\bar{x}$ $\sigma$	$\bar{x}$ $\sigma$	$\bar{x}$ $\sigma$	$\bar{x}$ $\sigma$	$\bar{x}$ $\sigma$	$\bar{x}$ $\sigma$	$\bar{x}$ $\sigma$	$\bar{x}$	$\bar{x}$	
wt%	SiO <sub>2</sub>	37.33 0.50	38.19 0.44	37.44 0.71	37.85 0.36	27.57 0.61	27.92 0.33	28.62 1.60	26.44 0.55	34.43 6.95	37.70 0.84	37.98 0.68	26.47	0.10	44.74 <sup>†</sup>	45.39 <sup>†</sup>	
	TiO <sub>2</sub>	bdl 0.01	bdl 0.01	bdl 0.01	bdl 0.01	0.18 0.14	0.11 0.04	0.17 0.11	bdl	0.06 0.10	bdl	bdl	bdl		bdl	bdl	
	Al <sub>2</sub> O <sub>3</sub>	28.39 0.25	30.14 0.17	28.46 0.44	28.90 0.22	21.41 0.12	20.98 0.17	21.19 0.54	21.71 0.33	25.01 3.68	32.06 0.56	32.27 0.26	22.83	0.12	38.92	36.39	
	FeO (T)	8.25 0.09	5.33 0.20	9.26 0.53	7.94 0.44	24.84 0.74	24.91 0.23	23.82 1.57	22.17 0.65	21.80 10.79	2.73 0.42	2.35 0.08	20.16	0.19	bdl	0.70	
	MnO	0.05 0.01	0.05 0.00	0.07 0.01	0.05 0.01	0.11 0.01	0.12 0.01	0.12 0.03	0.09 0.01	0.49 0.55	bdl	bdl	0.48	0.03	bdl	bdl	
	ZnO	nd	nd	nd	nd	bdl	0.03 0.03	0.05 0.03	bdl 0.03	0.01 0.01	bdl	bdl	bdl		bdl	bdl	
	MgO	7.37 0.28	6.76 0.25	8.77 0.63	9.28 0.20	13.91 0.42	14.64 0.31	14.25 0.97	16.71 0.56	7.80 2.67	12.31 0.73	12.29 0.85	16.60	0.19	15.87	16.89	
	CaO	0.32 0.09	0.34 0.02	0.42 0.07	0.46 0.00	bdl	bdl	bdl	bdl	0.11 0.18	0.09 0.13	bdl	bdl		bdl	bdl	
	Na <sub>2</sub> O	0.07 0.02	0.07 0.01	0.03 0.02	0.03 0.01	bdl	bdl	bdl	bdl	0.04 0.04	bdl	bdl	bdl		bdl	bdl	
	K <sub>2</sub> O*	2.62 0.39	2.11 0.12	1.51 0.59	0.82 0.12	0.30 0.29	0.19 0.14	0.63 0.71	bdl	2.93 2.95	0.89 0.20	0.89 0.24	0.02	0.01	0.46	0.63	
	Cl	nd	nd	nd	nd	bdl	bdl	bdl	0.03 0.01	0.04 0.03	0.03 0.01	0.03 0.01	bdl		bdl	bdl	
	F	nd	nd	nd	nd	0.13 0.02	0.17 0.06	0.21 0.04	0.09 0.04	0.10 0.09	0.07 0.02	0.03 0.02	0.06	0.04	bdl	bdl	
	Total	84.41 0.48	82.98 0.32	85.99 0.39	85.35 0.24	88.44 0.24	89.04 0.15	89.00 0.34	87.27 0.40	92.78 2.31	85.88 0.41	85.88 0.31	86.64	0.23	100.00	100.00	
	Fe/Fe+Mg	0.39	0.31	0.37	0.32	0.62	0.49	0.48	0.43	0.50	0.11	0.10	0.41				
apfu	Si	2.58	2.62	2.54	2.55	2.34	2.05	2.09	1.96	2.04	2.46	2.47	1.96		2.45	2.50	
	Al	2.31	2.43	2.27	2.30	2.02	1.82	1.83	1.90	1.87	2.46	2.47	1.99		2.52	2.36	
	Fe	0.48	0.31	0.52	0.45	1.31	1.53	1.46	1.38	1.54	0.15	0.13	1.25			0.03	
	Mn					0.03							0.03				
	Mg	0.76	0.69	0.89	0.93	0.81	1.60	1.56	1.85	1.53	1.20	1.19	1.83		1.30	1.39	
	K	0.02	0.02	0.03	0.03	0.24	0.02	0.06		0.03	0.07	0.07			0.05	0.07	
	F	0.23	0.18	0.13	0.07	0.02	0.04	0.05	0.02	0.03							
	O*	10.00	10.00	10.00	10.00	10.00	10.00	10.00	10.00	10.00	10.00	10.00	10.00		10.00	10.00	

<sup>†</sup>semi-quantified using SEM-EDS (normalized to 100% total); \*K<sub>2</sub>O is contamination of illite; nd= no data; bdl = below detection limits; BaO & SrO below detection limits; u/g = underground collared hole; FeO (T) = total Fe as FeO

Table 3: EMPA analyses of illite and kaolinite from background drill-hole MC344. Atoms per formula unit normalized to O = 10 for illite and O = 5 for kaolinite.

sample (dep	9 (628.2 m)		13 (525.9 m)				17 (499.4 m)								
lithology	<i>moderately chloritized metapelite</i>		<i>chloritized metapelite</i>				<i>basal quartzite</i>								
mineral	coarse-grained illite	fine-grained illite	fine-grained illite	illitized chloritized garnet			kaolinite lamella in illite		fine-grained kaolinite		coarse-grained illite				
	$\bar{x}$ $\sigma$	$\bar{x}$ $\sigma$	$\bar{x}$ $\sigma$	$\bar{x}$ $\sigma$	$\bar{x}$ $\sigma$	$\bar{x}$ $\sigma$	$\bar{x}$ $\sigma$	$\bar{x}$ $\sigma$	$\bar{x}$ $\sigma$	$\bar{x}$ $\sigma$	$\bar{x}$ $\sigma$	$\bar{x}$ $\sigma$	$\bar{x}$ $\sigma$	$\bar{x}$ $\sigma$	$\bar{x}$ $\sigma$
<i>wt%</i>															
SiO <sub>2</sub>	48.61 0.41	46.52 0.86	48.58 0.71	49.73 0.24	47.89 1.06	48.80 1.10	46.26 0.20	45.75 0.02	46.13 0.27	46.80 0.42	45.85 0.38	45.93 0.37	45.92 0.31	46.42 0.22	
TiO <sub>2</sub>	bdl	bdl	bdl 0.01	bdl	bdl	bdl	bdl	0.16 0.16	bdl	bdl	0.24 0.19	0.28 0.20	bdl	0.06 0.07	
Al <sub>2</sub> O <sub>3</sub>	31.50 0.22	31.75 0.31	32.54 0.30	32.22 0.34	33.57 0.40	32.64 0.57	37.01 0.49	35.57 1.16	37.09 1.45	37.46 0.41	35.68 0.78	36.11 0.85	37.66 0.38	37.16 0.60	
FeO (T)	2.63 0.24	2.28 0.64	2.04 0.40	1.49 0.11	1.94 0.64	1.81 0.31	0.18 0.03	0.41 0.23	0.15 0.08	0.12 0.05	0.78 0.17	0.75 0.20	0.11 0.04	0.50 0.35	
MgO	1.97 0.18	2.39 0.39	1.79 0.43	1.15 0.11	1.42 0.55	1.66 0.31	0.08 0.03	0.25 0.18	0.05 0.05	0.03 0.02	0.49 0.22	0.43 0.24	0.07 0.04	0.05 0.06	
Na <sub>2</sub> O	0.11 0.02	0.15 0.01	0.03 0.01	0.03 0.01	0.02 0.01	0.03 0.02	0.06 0.01	0.08 0.04	0.03 0.01	bdl	0.41 0.10	0.42 0.12	0.29 0.01	0.24 0.02	
K <sub>2</sub> O	10.05 0.24	9.16 0.24	9.80 0.63	9.77 0.10	9.69 0.73	9.26 0.63	1.93 0.20	3.98 1.25	1.02 0.69	0.82 0.24	10.96 0.23	10.95 0.14	10.98 0.07	10.50 0.91	
BaO	0.21 0.01	0.35 0.13	bdl	bdl	bdl	bdl	bdl	bdl	bdl	bdl	0.03 0.02	0.04 0.03	bdl	0.06 0.04	
F	0.22 0.06	0.17 0.05	0.08 0.04	0.15 0.04	0.06 0.07	0.12 0.05	0.08 0.10	0.04 0.04	0.11 0.06	0.08 0.07	0.08 0.04	0.07 0.04	0.04 0.04	0.06 0.04	
Total	95.29 0.34	92.76 0.22	94.89 0.55	94.55 0.36	94.61 0.95	94.34 0.45	85.61 0.40	86.28 0.62	84.58 0.66	85.34 0.42	94.54 0.26	94.99 0.20	95.13 0.38	95.05 0.86	
<i>apfu</i>															
Si	2.95	2.89	2.94	3.00	2.90	2.95	1.45	1.45	1.45	1.46	2.80	2.75	2.77	2.79	
Al	2.25	2.33	2.32	2.29	2.40	2.33	1.37	1.33	1.38	1.38	2.56	2.66	2.67	2.64	
Fe	0.13	0.12	0.10	0.08	0.10	0.09		0.01			0.04	0.03	0.01	0.03	
Mg	0.18	0.22	0.16	0.10	0.13	0.15		0.01			0.04	0.02	0.01		
Na											0.05	0.07	0.03	0.03	
K	0.78	0.73	0.76	0.75	0.75	0.71	0.07	0.16	0.04	0.03	0.85	0.84	0.84	0.81	
F	0.04	0.03	0.02	0.03	0.01	0.02			0.01	0.01	0.02	0.01	0.01	0.01	
O*	10	10	10	10	10	10	5	5	5	5	10	10	10	10	

MnO, CaO, ZnO, Cl & SrO below detection limits (bdl); FeO (T) = total Fe as FeO; \*O determined stoichiometrically

Table 4: EMPA analyses of illite from along the P2 fault. Atomic proportions are normalized to O = 10.

		MC370 (sub-ec P2)				MC349 (sub-ec P2)				MC361 (barren P2)				H201 (Zone 2)		MO227 (Zone 2)				H3559 (Zone 1)		H347 (Zone 2)					
		32 (543 m)				29 (560.2 m)				89 (645.5 m)				111 (581.6 m)		69 (w/g)		146 (w/g)				201 (w/g)		75 (w/g)			
		<i>sandstone</i>				<i>brecciated metapelite</i>												<i>metapelite</i>		<i>metapelite</i>				<i>graphitic metapelite</i>		<i>brecciated pegmatite</i>	
		<i>above unconformity</i>				<i>thrusted over sandstone</i>												<i>metapelite</i>						<i>metapelite</i>			
		$\bar{x}$	$\sigma$	$\bar{x}$	$\sigma$	$\bar{x}$	$\sigma$	$\bar{x}$	$\sigma$	$\bar{x}$	$\sigma$	$\bar{x}$	$\sigma$	$\bar{x}$	$\sigma$	$\bar{x}$	$\sigma$	$\bar{x}$	$\sigma$	$\bar{x}$	$\sigma$	$\bar{x}$	$\sigma$	$\bar{x}$	$\sigma$		
wt%	SiO <sub>2</sub>	44.81	0.36	46.07	0.15	45.79	0.45	45.27	0.53	46.67	2.70	46.82	1.19	45.99	0.17	41.89	3.98	43.86	0.33	44.67	0.60	45.13	0.63	46.33	0.92	47.53	0.45
	TiO <sub>2</sub>	0.98	0.04	0.99	0.02	0.08	0.01	0.10	0.03	0.22	0.20	0.04	0.03	0.02	0.01	0.05	0.03	0.27	0.10	0.03	0.01	0.03	0.01	0.01	0.01	0.01	0.01
	Al <sub>2</sub> O <sub>3</sub>	33.61	0.13	33.56	0.10	34.81	0.43	34.84	1.02	30.46	0.93	32.61	0.83	33.50	0.64	31.74	0.94	33.68	0.29	35.07	0.78	34.71	1.00	32.49	0.76	34.80	0.75
	FeO (T)	2.95	0.09	1.22	0.02	1.02	0.11	1.51	0.50	1.05	1.20	1.62	0.71	2.48	0.23	0.41	0.08	0.79	0.03	0.64	0.05	0.65	0.10	0.90	0.01	1.17	0.40
	MgO	0.56	0.07	1.07	0.02	0.86	0.18	1.29	0.47	5.89	2.56	2.01	0.50	1.08	0.31	9.03	3.36	0.40	0.10	0.59	0.29	0.46	0.26	1.15	0.35	0.20	0.11
	Na <sub>2</sub> O	0.47	0.05	0.40	0.01	0.34	0.05	0.33	0.04	0.03	0.01	0.17	0.03	0.21	0.02	0.04	0.01	0.39	0.04	0.32	0.07	0.33	0.12	0.08	0.00	0.20	0.09
	K <sub>2</sub> O	10.59	0.08	10.96	0.04	10.71	0.24	10.27	0.43	7.37	1.17	10.11	0.66	10.43	0.20	4.23	2.68	9.54	0.05	9.70	0.31	9.84	0.24	10.84	0.07	10.95	0.14
	Cl	bdl		bdl		bdl		0.10	0.09	bdl		0.10	0.07	0.13	0.02	0.07	0.01	bdl		bdl		bdl		bdl		bdl	
	BaO	0.45	0.18	0.03	0.03	0.12	0.04	0.12	0.04	0.01	0.01	0.15	0.09	0.17	0.06	0.01	0.02	0.01	0.01	0.01	0.01	0.01	0.02	0.09	0.03	0.06	0.04
	F	0.11	0.03	0.47	0.04	0.08	0.06	0.13	0.06	0.19	0.08	0.20	0.09	0.12	0.01	0.17	0.06	0.02	0.03	0.09	0.03	0.05	0.06	0.16	0.08	0.07	0.02
	Total	94.52	0.32	94.60	0.20	93.81	0.33	93.90	0.67	91.88	0.68	93.75	0.91	94.08	0.50	87.56	2.32	88.96	0.32	91.09	0.31	91.25	0.32	92.02	0.53	94.98	0.26
apfu:	Si	2.77		2.80		2.81		2.78		2.87		2.85		2.84		2.67		2.82		2.80		2.83		2.90		2.88	
	Al	2.45		2.41		2.52		2.52		2.21		2.41		2.44		2.38		2.55		2.59		2.56		2.40		2.48	
	Ti	0.05		0.05																							
	Fe	0.15		0.06		0.05		0.08		0.05		0.10		0.13		0.02		0.04		0.03		0.03		0.05		0.06	
	Mg	0.05		0.10		0.08		0.12		0.54		0.16		0.10		0.86		0.04		0.06		0.04		0.11		0.02	
	Na	0.06		0.05		0.04		0.04		0.00		0.02		0.03				0.05		0.04		0.04		0.01		0.02	
	K	0.84		0.85		0.84		0.80		0.58		0.82		0.82		0.34		0.78		0.78		0.79		0.87		0.85	
	F	0.02		0.09						0.04		0.04				0.03							0.03				
	O*	10		10		10		10		10		10.00		10.00		10		10.00		10.00		10.00		10.00		10.00	

MnO, CaO, ZnO, & SrO below detection limits (bdl); FeO (T) = total Fe as FeO; \*O determined stoichiometrically

Table 5: Chemical composition of dravite determined by EMPA and SEM† analysis. Atom proportions are O = 24.5 ((BO<sub>3</sub>)<sub>3</sub>O<sub>18</sub>(OH)<sub>4</sub>)

drill-hole sample (depth/ host rock)	H3559 (Zone 1) 201 (u/g) graphitic pelite								MC361 (barren)				MC349 (sub-economic) 99 (~578 m) brecciated metapelite				H493 (Zone 2) 85 (u/g) altered metapelite																						
									109 (587.6 m) pegmatite		111 (581.6 m) pegmatite																												
	$\bar{x}$	$\sigma$	$\bar{x}$	$\sigma$	$\bar{x}$	$\sigma$	$\bar{x}$	$\sigma$	$\bar{x}$	$\sigma$	$\bar{x}$	$\sigma$	$\bar{x}$	$\sigma$	$\bar{x}$	$\sigma$	$\bar{x}$	$\sigma$																					
wt%	SiO <sub>2</sub>	35.35	0.31	34.94	0.07	35.36	0.35	34.96	0.08	35.23	0.05	35.09	0.17	35.10	0.24	35.20	0.07	35.50	0.13	35.34	0.09	35.16	0.16	34.83	0.09	34.67	0.09	35.52	0.26	35.63	0.32	35.68	0.47	35.45	0.17	41.78†	0.55	40.39†	0.6
	TiO <sub>2</sub>	1.06	0.15	1.23	0.07	1.08	0.10	1.21	0.07	1.28	0.03	1.24	0.08	1.14	0.01	1.23	0.06	1.34	0.04	1.36	0.08	1.36	0.19	1.14	0.07	1.25	0.05	1.29	0.08	1.23	0.09	1.27	0.17	1.28	0.13	0.96	0.19	1.12	0.3
	Al <sub>2</sub> O <sub>3</sub>	32.06	0.15	32.20	0.23	31.76	0.22	31.75	0.16	31.88	0.24	32.05	0.19	32.54	0.13	31.98	0.09	31.65	0.23	31.75	0.15	32.02	0.14	32.30	0.06	32.21	0.16	31.83	0.19	31.80	0.13	31.68	0.27	31.94	0.23	38.32	0.92	39.05	0.7
	FeO (T)	3.56	0.02	3.63	0.15	3.57	0.10	3.50	0.11	3.40	0.19	3.58	0.14	3.67	0.11	3.69	0.08	4.78	0.04	4.77	0.02	5.32	0.12	5.14	0.01	5.26	0.04	4.68	0.18	4.90	0.02	4.78	0.16	4.87	0.00	7.79	0.57	12.18	0.9
	MnO	0.01	0.01	0.02	0.01	bdl		0.01	0.01	0.02	0.01	0.01	0.01	0.01	bdl			0.03	0.00	0.03	0.01	0.03	0.01	0.01	0.01	0.02	0.00	0.02	0.02	0.02	0.02	0.01	0.01	0.01	0.01	bdl		bdl	
	ZnO	0.01	0.01	0.01	0.01	0.01	0.02	0.01	0.01	0.01	0.01	0.01	0.02	0.01	0.01	0.01		0.01	0.02	0.00	0.01	0.01	0.01	0.03	0.03	0.02	0.02	0.01	0.02	0.02	0.01	0.02	0.01	0.01	0.01	bdl		bdl	
	MgO	8.34	0.06	8.34	0.06	8.32	0.04	8.40	0.07	8.34	0.08	8.31	0.03	8.16	0.08	8.26	0.06	7.74	0.07	7.63	0.04	7.15	0.19	7.10	0.03	7.05	0.06	7.68	0.06	7.73	0.04	7.62	0.09	7.51	0.04	7.86	0.48	5.09	0.5
	CaO	1.27	0.25	1.51	0.07	1.27	0.22	1.51	0.14	1.61	0.01	1.60	0.08	1.51	0.02	1.58	0.08	1.20	0.08	1.01	0.05	0.92	0.07	1.27	0.04	1.36	0.05	1.36	0.12	1.28	0.12	1.31	0.27	1.38	0.15	1.03	0.03	0.92	0.2
	Na <sub>2</sub> O	1.71	0.11	1.68	0.05	1.77	0.08	1.65	0.09	1.61	0.05	1.62	0.04	1.66	0.02	1.64	0.02	1.95	0.04	2.05	0.04	1.98	0.09	1.72	0.02	1.67	0.03	1.73	0.07	1.78	0.07	1.74	0.15	1.71	0.03	2.25	0.06	2.00	0.1
	K <sub>2</sub> O	0.07	0.01	0.07	0.01	0.06	0.01	0.07	0.00	0.08	0.01	0.08	0.00	0.08	0.01	0.07	0.00	0.07	0.00	0.07	0.01	0.06	0.01	0.08	0.01	0.08	0.01	0.07	0.01	0.06	0.02	0.07	0.02	0.07	0.01	bdl		bdl	
	BaO	0.01	0.01	0.03	0.04	0.03	0.01	0.00	0.00	0.02	0.02	0.01	0.01	0.02	0.01	0.01	0.01	0.02	0.03	0.02	0.02	0.02	0.02	0.01	0.01	0.02	0.01	0.01	0.01	0.01	0.01	0.01	0.00	0.00	bdl		bdl		
	F	0.42	0.03	0.45	0.06	0.41	0.04	0.41	0.01	0.44	0.07	0.54	0.05	0.47	0.02	0.50	0.03	0.25	0.06	0.22	0.08	0.25	0.05	0.39	0.08	0.45	0.07	0.57	0.08	0.44	0.06	0.53	0.07	0.54	0.07	bdl		bdl	
	SrO	bdl		bdl		bdl		bdl		bdl		0.02	0.02	bdl		bdl		0.01	0.02	0.01	0.01	bdl		0.01	0.01	0.01	0.01	0.02	0.02	bdl	0.03	0.04	0.03	0.04	bdl		bdl		
	Total	83.70	0.22	83.93	0.18	83.47	0.07	83.31	0.14	83.75	0.31	83.93	0.16	84.19	0.18	83.98	0.07	84.45	0.21	84.15	0.13	84.18	0.26	83.86	0.06	83.88	0.21	84.56	0.13	84.76	0.23	84.52	0.18	84.58	0.06	100.00		100.00	
	F/Cl	134		1513		443		497		332		266		1444		bdl		173		246		98		278		245		557		564		1496		10876					
<i>apfu</i>																																							
	T:	Si	5.75	5.69	5.77	5.72	5.74	5.71	5.69	5.73		5.77	5.76	5.74	5.71	5.69	5.77	5.77	5.77	5.77	5.79	5.76		5.77	5.77	5.79	5.76												
		Al	0.25	0.31	0.23	0.28	0.26	0.29	0.31	0.27		0.23	0.24	0.26	0.29	0.31	0.23	0.23	0.23	0.23	0.21	0.24		0.23	0.23	0.21	0.24												
	Z:	Al	5.90	5.86	5.88	5.85	5.85	5.86	5.91	5.86		5.82	5.85	5.90	5.95	5.92	5.86	5.82	5.85	5.90	5.95	5.92		5.86	5.84	5.86	5.87												
		Fe	0.10	0.14	0.12	0.15	0.15	0.14	0.09	0.14		0.18	0.15	0.10	0.05	0.08	0.14	0.18	0.15	0.10	0.05	0.08		0.14	0.16	0.14	0.13												
	Y:	Fe	0.39	0.36	0.37	0.33	0.32	0.35	0.41	0.36		0.47	0.50	0.62	0.65	0.64	0.49	0.47	0.50	0.62	0.65	0.64		0.49	0.51	0.51	0.53												
		Ti	0.13	0.15	0.13	0.15	0.16	0.15	0.14	0.15		0.16	0.17	0.17	0.14	0.15	0.16	0.16	0.16	0.17	0.17	0.14	0.15		0.16	0.15	0.15	0.16											
		Mg	2.02	2.02	2.02	2.05	2.02	2.02	1.97	2.00		1.87	1.85	1.74	1.73	1.72	1.86	1.87	1.85	1.74	1.73	1.72		1.86	1.87	1.84	1.82												
		Ca	0.22	0.26	0.22	0.26	0.28	0.28	0.26	0.28		0.21	0.18	0.16	0.22	0.24	0.24	0.24	0.22	0.18	0.16	0.22	0.24		0.24	0.22	0.23	0.24											
		□	0.24	0.20	0.25	0.21	0.22	0.21	0.21	0.21		0.28	0.31	0.31	0.25	0.24	0.26	0.26	0.28	0.31	0.31	0.25	0.24		0.26	0.25	0.27	0.25											
	X:	Na	0.54	0.53	0.56	0.52	0.51	0.51	0.52	0.52		0.62	0.65	0.63	0.55	0.53	0.55	0.62	0.65	0.63	0.55	0.53		0.55	0.56	0.55	0.54												
		K	0.01	0.02	0.01	0.01	0.02	0.02	0.02	0.02		0.02	0.01	0.01	0.02	0.02	0.02	0.02	0.02	0.01	0.01	0.02	0.02		0.02	0.01	0.02	0.01											
		□	0.44	0.45	0.43	0.46	0.48	0.47	0.46	0.47		0.37	0.34	0.36	0.44	0.45	0.44	0.37	0.34	0.36	0.44	0.45		0.44	0.43	0.44	0.45												
	B:	B*	3.00																																				
	O:	O*	24.5	24.5	24.5	24.5	24.5	24.5	24.5	24.5		24.5	24.5	24.5	24.5	24.5	24.5	24.5	24.5	24.5	24.5	24.5		24.5	24.5	24.5	24.5												
		OH <sup>+</sup>	3.79	3.77	3.79	3.79	3.78	3.73	3.76	3.75		3.87	3.89	3.87	3.80	3.77	3.71	3.87	3.89	3.87	3.80	3.77		3.71	3.77	3.73	3.73												
		F	0.21	0.23	0.21	0.21	0.22	0.27	0.24	0.25		0.13	0.11	0.13	0.27	0.23	0.29	0.13	0.11	0.13	0.27	0.23		0.29	0.23	0.27	0.27												

□ = vacancy; \* determined by stoichiometry; FeO (T) = total Fe; †SEM analysis of green altered dravite (normalized to 100% total) see Fig. 7-F2

Table 6: EMPA analyses of magnesiofioite from basement rocks and sandstone along the P2 Fault. Atom proportions are normalized to O = 24.5 ((BO<sub>3</sub>)<sub>2</sub>O)<sub>18</sub>(OH)<sub>4</sub>.

drill-hole	MC349 (sub-ec)				MC362 (barren)	MC370 (sub-ec)			H201 (Zone 2)						H3559 (Zone 1)				MO227 (Zone 2)																							
sample (depth)	89 (645.5 m)				122 (637.9 m)	29 (560.2 m)	32 (543 m)			69 (u/g)			70 (u/g)			201 (Zone 1 underground)				146 (u/g)																						
rock	quartz-rich altered pegmatite				brecciated metapelite	bleached SS above u/c	brecciated metapelite	bleached SS above u/c			altered metapelite			altered metapelite			graphitic graphitic pelite				metapelite																					
EMPA data	$\bar{x}$	$\sigma$	$\bar{x}$	$\sigma$	$\bar{x}$	$\bar{x}$	$\sigma$	$\bar{x}$	$\sigma$	$\bar{x}$	$\sigma$	$\bar{x}$	$\sigma$	$\bar{x}$	$\sigma$	$\bar{x}$	$\sigma$	$\bar{x}$	$\sigma$	$\bar{x}$	$\sigma$																					
wt% SiO <sub>2</sub>	37.39	0.21	37.65	0.29	37.51	0.59	33.89	2.32	34.37	0.29	35.94	0.35	32.97	0.28	34.07	0.93	37.23	0.14	36.62	0.58	36.11	0.23	36.12	0.29	36.52	0.72	36.83	0.75	36.81	0.60	35.68	3.31	37.12	0.54	36.13	1.09	36.68	0.54	35.03	1.22		
Al <sub>2</sub> O <sub>3</sub>	35.47	0.14	35.31	0.17	35.45	0.66	30.69	2.54	33.29	0.91	36.85	0.63	38.21	0.22	37.67	0.32	35.36	0.22	35.90	0.44	35.49	0.23	35.02	0.24	35.35	0.21	36.15	0.42	35.88	0.54	34.06	1.25	34.47	0.66	32.79	0.44	33.30	0.56	34.85	0.88		
FeO	0.14	0.03	0.14	0.01	0.10	0.04	1.39	0.14	2.10	0.20	1.21	0.07	0.69	0.04	0.86	0.11	0.12	0.02	0.13	0.04	0.13	0.02	0.16	0.02	0.11	0.03	0.09	0.02	0.10	0.03	0.20	0.02	0.20	0.03	0.26	0.05	0.23	0.05	1.45	0.33		
MgO	8.52	0.10	8.56	0.12	8.64	0.21	6.67	0.53	6.96	0.04	7.88	0.12	7.43	0.14	7.39	0.11	8.74	0.05	8.50	0.07	8.62	0.05	8.77	0.16	8.39	0.08	8.40	0.10	8.47	0.13	8.11	0.80	8.35	0.17	8.37	0.34	8.42	0.32	7.26	0.20		
CaO	0.11	0.01	0.11	0.01	0.03	0.02	0.07	0.01	0.05	0.01	0.09	0.01	0.25	0.03	0.22	0.04	0.10	0.02	0.13	0.03	0.10	0.01	0.09	0.02	0.11	0.01	0.12	0.02	0.11	0.02	0.02	0.01	0.02	0.01	0.02	0.00	0.02	0.02	0.11	0.04		
Na <sub>2</sub> O	0.79	0.07	0.79	0.05	0.57	0.14	0.74	0.08	0.83	0.07	0.55	0.08	0.44	0.02	0.55	0.05	0.68	0.03	0.64	0.07	0.62	0.05	0.60	0.02	0.64	0.07	0.59	0.09	0.61	0.06	0.59	0.04	0.59	0.07	0.67	0.06	0.61	0.08	0.73	0.21		
K <sub>2</sub> O	0.02	0.02	0.02	0.01	0.01	0.01	0.02	0.02	bdl		0.01	0.01	0.00	0.00	0.01	0.01	0.04	0.02	0.02	0.01	0.03	0.01	0.04	0.02	0.02	0.01	0.06	0.08	0.03	0.01	bdl	0.02	0.01	bdl	bdl	bdl	bdl	bdl	bdl	0.02	0.02	
Cl	0.01	0.00	0.02	0.00	bdl		bdl		bdl		0.01	0.00	0.01	0.00	0.01	0.00	0.03	0.01	0.02	0.01	0.02	0.01	0.03	0.01	0.01	0.00	0.01	0.00	0.02	0.00	bdl	bdl										
F	0.05	0.03	0.05	0.05	0.02	0.02	0.31	0.13	0.18	0.09	0.05	0.03	0.04	0.05	0.08	0.04	0.12	0.03	0.08	0.04	0.08	0.03	0.05	0.03	0.06	0.04	0.06	0.06	0.06	0.03	0.14	0.22	0.03	0.05	0.04	0.04	0.05	0.02	0.04	0.02		
SrO	bdl		bdl		0.01	0.02	bdl		0.03	0.04	bdl		bdl		0.02	0.02	0.01	0.01	bdl		bdl		0.02	0.02	0.02	0.02	bdl		0.02	0.02	bdl	bdl	bdl	bdl	0.02	0.03	bdl	bdl	bdl	bdl		
Total	82.52	0.29	82.66	0.28	82.35	0.63	73.69	5.25	77.77	0.93	82.64	0.43	80.03	0.39	80.86	0.84	82.38	0.26	82.03	0.36	81.20	0.26	80.91	0.31	81.23	0.75	82.32	0.57	82.12	0.31	78.79	5.22	80.82	1.40	78.33	1.82	79.34	0.78	79.51	1.51		
F/Cl	5		3				24				17		6		8		4		3		8		3		8		11		6										12			
apfu: T:	Si	5.93	5.96	5.95	6.07	5.87	5.73	5.42	5.54	5.90	5.84	5.83	5.85	5.88	5.86	5.87	5.92	6.00	6.04	6.04	6.04	5.81	0.19																			
	Al	0.07	0.04	0.05		0.13	0.27	0.58	0.46	0.10	0.16	0.17	0.15	0.12	0.14	0.13	0.08																									
Z	Al	6	6	6	6	6	6	6	6	6	6	6	6	6	6	6	6	6	6	6	6	6	6	6	6	6	6	6	6	6	6	6	6	6	6	6	6	6	6	6	6	
Y:	Al	0.55	0.54	0.58	0.48	0.56	0.66	0.82	0.77	0.52	0.58	0.58	0.54	0.60	0.63	0.61	0.60	0.57	0.46	0.47	0.64	0.64	0.64	0.64	0.60	0.57	0.46	0.47	0.64	0.64	0.64	0.64	0.64	0.64	0.64	0.64	0.64	0.64	0.64	0.64	0.64	0.64
	Mg	2.01	2.02	2.04	1.78	1.77	1.87	1.82	1.79	2.07	2.02	2.08	2.12	2.01	1.99	2.01	2.00	2.01	2.08	2.07	1.80	1.80	1.80	1.80	2.01	2.01	2.08	2.07	1.80	1.80	1.80	1.80	1.80	1.80	1.80	1.80	1.80	1.80	1.80	1.80	1.80	
	Fe	0.02	0.02	0.01	0.21	0.30	0.16	0.10	0.12	0.02	0.02	0.02	0.02	0.01	0.01	0.01	0.03	0.03	0.04	0.03	0.20	0.20	0.20	0.20	0.02	0.02	0.02	0.02	0.02	0.02	0.02	0.02	0.02	0.02	0.02	0.02	0.02	0.02	0.02	0.02	0.02	0.02
	Ca	0.02	0.02	0.01	0.01	0.01	0.02	0.04	0.04	0.02	0.02	0.02	0.02	0.02	0.02	0.02	0.36	0.39	0.42	0.43	0.02	0.02	0.02	0.02	0.02	0.02	0.02	0.02	0.02	0.02	0.02	0.02	0.02	0.02	0.02	0.02	0.02	0.02	0.02	0.02	0.02	
	□	0.39	0.40	0.36	0.52	0.36	0.29	0.22	0.29	0.39	0.36	0.31	0.30	0.35	0.35	0.34	0.36	0.39	0.42	0.43	0.02	0.02	0.02	0.02	0.35	0.35	0.34	0.36	0.39	0.42	0.43	0.36	0.39	0.42	0.43	0.36	0.39	0.42	0.43	0.36	0.39	
X:	Na	0.24	0.24	0.18	0.26	0.26	0.17	0.14	0.17	0.21	0.20	0.19	0.19	0.20	0.18	0.19	0.19	0.18	0.22	0.19	0.23	0.23	0.23	0.23	0.20	0.18	0.22	0.19	0.19	0.19	0.19	0.18	0.18	0.22	0.19	0.19	0.19	0.19	0.19	0.19	0.19	
	K						0.01			0.01																																
	□	0.76	0.76	0.82	0.74	0.74	0.83	0.86	0.83	0.78	0.80	0.81	0.81	0.80	0.81	0.80	0.81	0.82	0.78	0.81	0.77	0.77	0.77	0.77	0.80	0.81	0.80	0.81	0.80	0.81	0.82	0.78	0.81	0.81	0.81	0.81	0.81	0.81	0.81	0.81		
B:	B*	3.00	3.00	3.00	3.00	3	3.00	3.00	3.00	3.00	3.00	3.00	3.00	3.00	3.00	3.00	3.00	3.00	3.00	3.00	3.00	3.00	3.00	3.00	3.00	3.00	3.00	3.00	3.00	3.00	3.00	3.00	3.00	3.00	3.00	3.00	3.00	3.00	3.00	3.00		
O:	O*	24.5	24.5	24.5	24.5	24.5	24.5	24.5	24.5	24.5	24.5	24.5	24.5	24.5	24.5	24.5	24.5	24.5	24.5	24.5	24.5	24.5	24.5	24.5	24.5	24.5	24.5	24.5	24.5	24.5	24.5	24.5	24.5	24.5	24.5	24.5	24.5	24.5	24.5	24.5	24.5	
	OH*	3.97	3.97	3.99	3.82	3.90	3.97	3.98	3.95	3.93	3.95	3.96	3.97	3.97	3.97	3.97	3.92	3.98	3.98	3.97	3.99	3.99	3.99	3.99	3.97	3.97	3.97	3.97	3.97	3.92	3.98	3.98	3.98	3.97	3.97	3.97	3.97	3.97	3.97	3.97		
	F	0.03	0.03	0.01	0.18	0.10	0.03	0.02	0.04	0.06	0.04	0.04	0.03	0.03	0.03	0.03	0.08	0.02	0.02	0.03	0.01	0.01	0.01	0.01	0.03	0.03	0.03	0.03	0.03	0.08	0.02	0.02	0.02	0.03	0.03	0.03	0.03	0.03	0.03			

□ = vacancy; u/c = unconformity; u/g = unground collared hole; \* determined by stoichiometry; FeO (T) = total Fe; \*OH & B calculated by stoichiometry; Ba, Ti, Mn, Zn are below detection limits of 0.01%